LUND UNIVERSITY

Approximative computation methods for monostatic scattering from axially symmetric objects

Ericsson, Andreas; Sjöberg, Daniel; Larsson, Christer; Martin, Torleif

2017

Total number of authors:
4

Approximative computation methods for monostatic scattering from axially symmetric objects

Andreas Ericsson, Daniel Sjöberg, Christer Larsson and Torleif Martin

Andreas Ericsson
andreas.ericsson@eit.lth.se

Daniel Sjöberg
daniel.sjoberg@eit.lth.se

†Christer Larsson
christer.larsson@eit.lth.se

†Torleif Martin
torleif.martin@eit.lth.se

Department of Electrical and Information Technology
Electromagnetic Theory
Lund University
P.O. Box 118
SE-221 00 Lund
Sweden

† also at
Saab
SE-581-88 Linköping
Sweden

Abstract

Two approximation methods are presented for fast calculations of the monostatic scattering from axial-symmetric scatterers coated with electromagnetic absorbers. The methods are designed for plane wave illumination parallel to the axis of rotation of the scatterer. The first method is based on simulating the scattering of a perfect electric conductor (PEC) enclosing the absorber coated scatterer, and multiplying the result with the squared magnitude of the absorber reflection coefficient in a planar scenario. The second method is based on simulating the scattering scenario in a physical optics (PO) solver, where the electromagnetic absorber is treated as reflection dyadic at the outer surface of the scatterer. Both methods result in a significant acceleration in computation speed in comparison to full wave methods, where the PO method carries out the computations in a number of seconds. The monostatic scattering from different geometries have been investigated, and parametric sweeps were carried out to test the limits where the methods yield accurate results. For specular reflections, the approximation methods yield very accurate results compared to full wave simulations when the radius of curvature is on the order of half a wavelength or larger of the incident signal. It is also concluded that the accuracy of the two methods vary depending on what type of absorber is applied to the scatterer, and that absorbers based on "volume losses" such as carbon doped foam absorber and thin magnetic absorbers yield better results than absorbers based on resistive sheets, such as a Salisbury absorber.

1 Introduction

In many applications it is of great interest to characterize how electromagnetic waves interact with objects [3]. In some scenarios this interaction should be as significant as possible, such as for antennas [2], while in other scenarios this interaction is to be minimized, such as in defense applications [25]. In order to minimize the electromagnetic scattering from an object one can either shape the object to direct the signals in desired directions, or use electromagnetic absorbers that reduce the electromagnetic scattering in a desired frequency band of operation [20].

When numerically calculating the scattered fields of an object, accurate results can be achieved using full wave methods such as the method of moments (MoM), finite element method (FEM), or finite difference time domain method (FDTD) [7, 16]. However, the computational requirements increase rapidly as the size of the scatterer is made larger than a few wavelengths in size [7]. In [4] it is shown that, in a simulation at the wave frequency f of a 3D system of fixed spatial extent, the number of floating point operations and the memory requirements scales as $\mathcal{O}(f^4)$ in all of the above mentioned methods. If a 2D simulation system is considered the MoM scales as $\mathcal{O}(f^2)$ and the FEM and FDTD scales as $\mathcal{O}(f^3)$ [4]. It should be noted that time-domain difference methods give a complete frequency spectrum, as compared to a standard frequency-domain method that requires one computation for a single frequency. This means that for wideband problems a time domain method can lead to reduced simulation complexity. In order to reduce the requirements and accelerate

simulations a number of numerical acceleration methods have been presented in the last decades. For MoM two such methods well suided for simulating electrically large scattering problems are the multilevel fast multipole method (MLFMM) [6, 8, 24] and the characteristic basis function method (CBF) [15, 21, 22]. The MLFMM scales in 3D as $\mathcal{O}(f^2\log(f))$ [4] which is a significant improvement, but can still result in heavy computations for complicated structures.

If for example an electromagnetic absorber consisting of single/multiple layers of different materials are applied to a scatterer under test the computational requirements increase even further, resulting in even higher memory requirements and longer simulation times [20]. A different approach to further reduce the computational requirements is to utilize high frequency approximation methods. This type of methods are commonly utilized when simulating very large objects, but can be useful for smaller scatterers as well. A high frequency approximation method used in many applications such as optics, electrical engineering and applied physics is physical optics (PO) [28]. It is an intermediate method between geometrical optics, which treats electromagnetic waves as rays, and full wave electromagnetism [7, 17]. The approximation consists of estimating the field on a surface using ray optics and then integrating the field over the surface to calculate the transmitted or scattered field. This resembles the Born approximation from the fact that details of the problem are treated as a perturbation [5]. A strong advantage of this method is the fact that the simulation complexity and computation time does not significantly increase with frequency as in the previous methods [1, 13, 29]. Drawback with PO is that it does not consider edgediffraction and the accuracy of the method is decreased for scattering in directions other than the specular direction [1]. Modified versions of PO have been presented throughout the years where these problem have been successfully addressed, utilizing physical theory of diffraction (PTD) or other techniques [23, 26, 30, 31, 32].

In this work, two approximation methods are presented for calculating the monostatic scattering from absorber coated axially-symmetric scatterers illuminated by a plane wave propagating along the axis of rotation of the scatterer. The methods are based on the work presented in [10, 12] where the effect of curvature on electromagnetic absorbers was evaluated using analytic recursion expressions. The first method consists in multiplying the scattering from a perfect electric conductor (PEC) enclosing the scatterer with the squared magnitude of the reflection coefficient of the absorber in a planar scenario. The second consists of calculating the monostatic scattering using the PO approximation, where the absorber is treated as an angle of incidence dependent reflection dyadic at the surface of the scatterer. An in-house solver presented in [27] is utilized for generating the PO simulation data, and is benchmarked against full wave simulations in Comsol Multiphysics. The time convention $e^{j\omega t}$ is used throughout this work.

This work is organized as follows: Simplified integral expressions for calculating the monostatic far field in a full wave- or PO solver are presented in Section 2. In Section 3 the approximation methods are introduced in detail and in Section 4 simulation results are presented for different electromagnetic absorbers used in this work. The two approximation methods are compared to a corresponding full wave

simulation for different electromagnetic absorbers applied to scatterers of different geometrical shapes in Section 5. Finally, a short summary and evaluation of the performance of the approximation methods are presented in Section 6, followed by some concluding remarks in Section 7.

2 Monostatic RCS from Axially Symmetric Scatterers

2.1 General formulation

In this work the main focus is on characterizing the monostatic radar cross section (RCS) from axially symmetric scatterers, illuminated along the axis of rotation. The RCS can be determined from the far field amplitude in the backscattering direction through the relation

$$\sigma = 4\pi \frac{|\boldsymbol{F}(-\hat{\boldsymbol{z}})|^2}{|E_0|^2}, \tag{2.1}$$

where σ is the RCS and E_0 is the amplitude of the incident electric field. In [27] a method was presented to determine the far field amplitude in the backscattering direction from a axially symmetric scatterer, illuminated by a linearly polarized (LP) plane wave $\boldsymbol{E}_0 = E_0 \mathrm{e}^{-\mathrm{j}kz}\hat{\boldsymbol{x}}$ propagating along the axis of rotation of the scatterer, as in Figure 1. There it was shown that by exciting the structure with a circularly polarized (CP) plane wave $\boldsymbol{E}_0 = E_0 \mathrm{e}^{-\mathrm{j}kz}\mathrm{e}^{\mp m\mathrm{j}\varphi}(\hat{\boldsymbol{\rho}} - \mathrm{j}\hat{\boldsymbol{\varphi}})$ of one of the two azimutal modes $m = \pm 1$, the backscattered farfield $\boldsymbol{F}(-\hat{\boldsymbol{z}})$ from the scatterer, illuminated by a LP plane wave, can be determined through the expression

$$\boldsymbol{F}(-\hat{\boldsymbol{z}}) = \hat{\boldsymbol{x}}\frac{\mathrm{j}k}{4}\int_\gamma \Big[n_\rho E_z(\rho, z) - n_z E_\rho(\rho, z) + \eta_0 n_z H_\varphi(\rho, z)$$
$$- \mathrm{j}n_z E_\varphi(\rho, z) + \mathrm{j}\eta_0(n_\rho H_z(\rho, z) - n_z H_\rho(\rho, z)) \Big]\mathrm{e}^{-\mathrm{j}kz}\rho\,\mathrm{d}\ell, \quad (2.2)$$

where the index $m = \pm 1$ has been dropped for brevity, k is the wave number, η_0 is the wave impedance in vacuum, $\hat{\boldsymbol{n}} = n_\rho\hat{\boldsymbol{\rho}} + n_z\hat{\boldsymbol{z}}$ is the normal vector of the scatterer, and the field components $(E_\rho, E_\varphi, E_z, H_\rho, H_\varphi, H_z)$ are computed in a numerical software and integrated over any given line segment γ enclosing the scatterer. In the following, we show how the electric and magnetic field components can be determined in the physical optics (PO) approximation, and how the expression (2.2) is reformulated in the PO scheme.

2.2 Physical optics formulation

In the PO approximation, the scattering surface is assumed to be locally flat [1, 29] and described by a reflection dyadic so that the tangential electric and magnetic
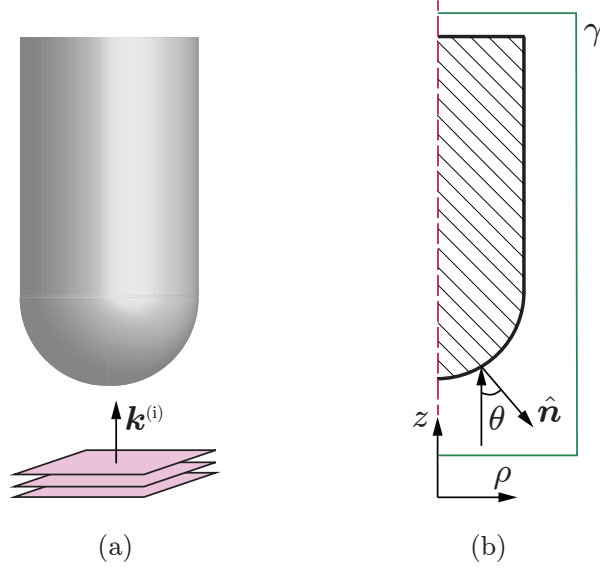
Figure 1: Principle sketch of a scattering scenario considered in this work. To the left a axially symmetric scatterer is illuminated by a plane wave along its axis of rotation. To the right a sketch of the numerical modeling of the scatterer is depicted, where the backscattered far field amplitude is calculated by calculating (2.2) along any line segment γ enclosing the scatterer.

fields are given by

$$\boldsymbol{E}_{\mathrm{t}} = (\mathbf{I} + \mathbf{R}) \cdot \boldsymbol{E}_{\mathrm{t}}^{(\mathrm{i})}, \tag{2.3}$$

$$\boldsymbol{H}_{\mathrm{t}} = \mathbf{Y}_{\mathrm{w}} \cdot (\mathbf{I} - \mathbf{R}) \cdot \boldsymbol{E}_{\mathrm{t}}^{(\mathrm{i})}. \tag{2.4}$$

By defining the unit vectors $\hat{\boldsymbol{p}}$ and $\hat{\boldsymbol{s}}$ spanning the surface, the identity dyadic in the tangential plane of the surface can be written as $\mathbf{I} = \hat{\boldsymbol{p}}\hat{\boldsymbol{p}} + \hat{\boldsymbol{s}}\hat{\boldsymbol{s}}$ and $\mathbf{R}$ denotes the reflection dyadic. The wave admittance dyadic of the surrounding medium $\mathbf{Y}_{\mathrm{w}}$ is defined as follows. A plane wave propagating in free space in the $\hat{\boldsymbol{k}}$ direction is given by the right-hand rule as $\boldsymbol{E} = \boldsymbol{E}_0 \mathrm{e}^{-\mathrm{j}k\hat{\boldsymbol{k}}\cdot\boldsymbol{r}}$ and $\boldsymbol{H} = \eta_0^{-1}\hat{\boldsymbol{k}} \times \boldsymbol{E}_0 \mathrm{e}^{-\mathrm{j}k\hat{\boldsymbol{k}}\cdot\boldsymbol{r}}$. Now fix a different direction $\hat{\boldsymbol{u}}$, and consider the components of $\boldsymbol{E}$ and $\boldsymbol{H}$ orthogonal to $\hat{\boldsymbol{u}}$ (the transverse parts, $\boldsymbol{E}_{\mathrm{t}}$ and $\boldsymbol{H}_{\mathrm{t}}$). The wave admittance is then defined by the relation $\boldsymbol{H}_{\mathrm{t}} = \mathrm{sign}(\hat{\boldsymbol{u}} \cdot \hat{\boldsymbol{k}})\mathbf{Y}_{\mathrm{w}} \cdot \boldsymbol{E}_{\mathrm{t}}$. In this case, it can be represented as (with $\hat{\boldsymbol{u}} = -\hat{\boldsymbol{n}}$ and assuming $(\hat{\boldsymbol{p}}, \hat{\boldsymbol{s}}, \hat{\boldsymbol{n}})$ is a right-handed system and $\hat{\boldsymbol{n}}$ is the outward pointing normal)

$$\mathbf{Y}_{\mathrm{w}} = -\hat{\boldsymbol{n}} \times \eta_0^{-1}\left(\frac{1}{\cos\theta}\hat{\boldsymbol{p}}\hat{\boldsymbol{p}} + \cos\theta\,\hat{\boldsymbol{s}}\hat{\boldsymbol{s}}\right) = \eta_0^{-1}\left(\frac{-1}{\cos\theta}\hat{\boldsymbol{s}}\hat{\boldsymbol{p}} + \cos\theta\,\hat{\boldsymbol{p}}\hat{\boldsymbol{s}}\right). \tag{2.5}$$

Here, θ is the angle of incidence. For an isotropic case, the reflection dyadic can be represented as

$$\mathbf{R} = R_{\mathrm{TM}}(\theta)\hat{\boldsymbol{p}}\hat{\boldsymbol{p}} + R_{\mathrm{TE}}(\theta)\hat{\boldsymbol{s}}\hat{\boldsymbol{s}} \tag{2.6}$$

and we have the result

$$\boldsymbol{E}_{\mathrm{t}} = (1 + R_{\mathrm{TM}}(\theta))E_{\mathrm{TM}}^{(\mathrm{i})}\hat{\boldsymbol{p}} + (1 + R_{\mathrm{TE}}(\theta))E_{\mathrm{TE}}^{(\mathrm{i})}\hat{\boldsymbol{s}}, \tag{2.7}$$

$$\boldsymbol{H}_{\mathrm{t}} = -\frac{\eta_0^{-1}}{\cos\theta}(1 - R_{\mathrm{TM}}(\theta))E_{\mathrm{TM}}^{(\mathrm{i})}\hat{\boldsymbol{s}} + \eta_0^{-1}\cos\theta(1 - R_{\mathrm{TE}}(\theta))E_{\mathrm{TE}}^{(\mathrm{i})}\hat{\boldsymbol{p}}. \tag{2.8}$$
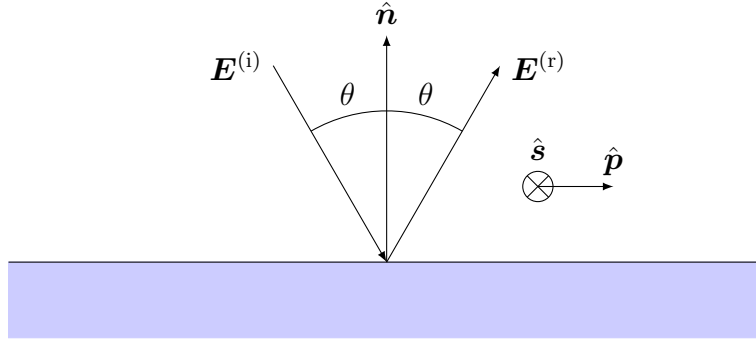
Figure 2: Local geometry of the plane of incidence, defining the unit vectors $\hat{\boldsymbol{p}}$ (corresponding to TM polarization) and $\hat{\boldsymbol{s}}$ (corresponding to TE polarization).

In [27] the tangential field components in the PO approximation in (2.7)-(2.8) are identified and reformulated on the form of the components in the integral (2.2), and the final result for the backscattered far field from a axially symmetric scatterer illuminated by a plane wave in the axial direction is

$$\boldsymbol{F}(-\hat{\boldsymbol{z}}) = -\hat{\boldsymbol{x}}\frac{\mathrm{j}k}{4}\int_\gamma \left[(1+R_{\mathrm{TM}})n_z + \frac{1-R_{\mathrm{TM}}}{\cos\theta}n_z^2 + (1+R_{\mathrm{TE}})n_z + \cos\theta(1-R_{\mathrm{TE}}) \right] E_0 \mathrm{e}^{-2\mathrm{j}kz}\rho\,\mathrm{d}\ell.$$
(2.9)

All parameters inside the integral can be parametrized along the curve γ. It is immediately seen that sections of a straight circular cylinder, where $n_z = 0$ and $\cos\theta = 0$, give zero contribution regardless of the reflection coefficients. In the next section, the relations (2.2) and (2.9) are used to calculate approximative results of the RCS of a scatterer coated by an electromagnetic absorber.

3 Approximative Computation Methods for Coated Scatterers

Two approximative computation methods for calculating the RCS from axially symmetric scatterers coated with an electromagnetic absorber are presented in this work. Both methods are based on the results presented in [10]. There it is shown that for a PEC sphere coated with an electromagnetic absorber an approximative relation is observed as the radius of the inner sphere is increased to a few wavelengths in size

$$\frac{\sigma^{\mathrm{coated}}}{\sigma^{\mathrm{PEC}}} \approx |S_{11}^{\mathrm{planar}}|^2,$$
(3.1)

where σ^{coated} is the RCS of the PEC sphere with an absorber, σ^{PEC} is the is the RCS from either the uncoated PEC sphere or a PEC sphere enclosing the coated scatterer, and S_{11}^{planar} is the reflection coefficient of the absorber, illuminated by a plane wave at normal incidence, in a planar scenario of infinite extent backed by ground plane, *i.e.* $S_{11}^{\mathrm{planar}} = \varGamma^{\mathrm{planar}}$. In [10] this relation was used to evaluate the
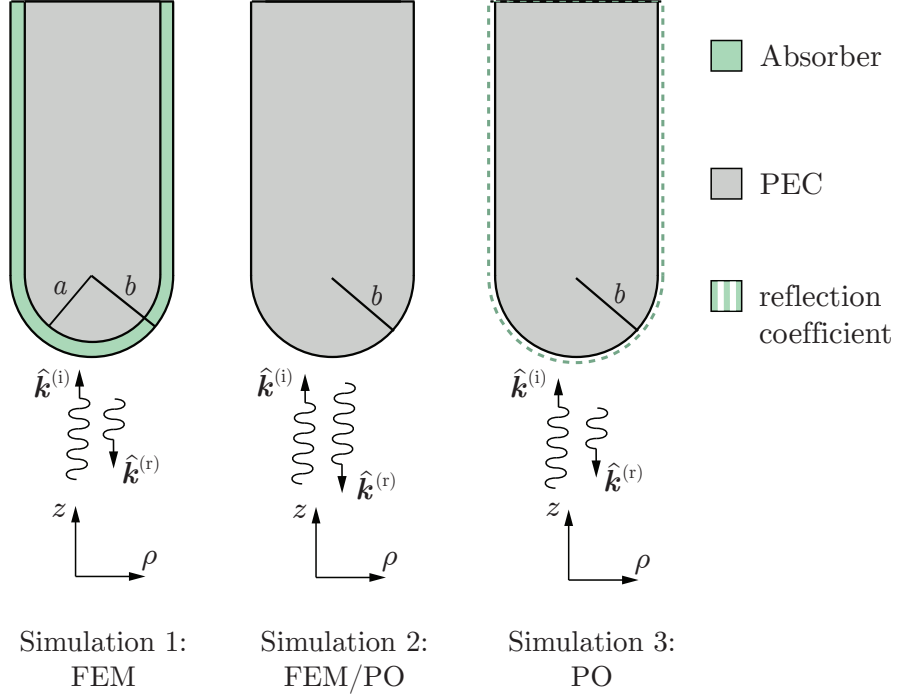
Figure 3: Three different RCS simulation cases evaluated for each geometry coated with a specific absorber. The left scenario shows the RCS of a full wave simulation model where the absorber is completely resolved in the meshing of the scatterer. The middle scenario depicts the RCS from a PEC enclosing the coated scatterer, which could be evaluated either using a full wave software or a PO solver. To the right the RCS of the coated scatterer is evaluated using a PO solver, where the absorber is treated as a reflection coefficient at the enclosing surface of the scatterer.

effect of curvature on the performance of different types of absorbers, and it was concluded that absorbers based on bulk loss, such as thin magnetic absorbers or carbon loaded foam absorbers, are less sensitive to curvature than absorbers based on single or multiple layers of resistive sheets. However, if (3.1) is rearranged we get the expression

$$\sigma^{\text{coated}} \approx \sigma^{\text{PEC}} |S_{11}^{\text{planar}}|^2 \tag{3.2}$$

which can be interpreted in the following way: the RCS from a PEC scatterer coated with an absorber can be approximated by the RCS from an enclosing PEC scatterer multiplied by the squared reflection coefficient of the absorber in a planar scenario. This relation is the first RCS approximation method used in this work, where the parameter σ^{PEC} could be determined either using a full wave simulation software, or a PO solver. This is depicted in the center illustration in Figure 3.

The second approximation method for calculating RCS in this work is based on evaluating (2.9) using an in-house PO code. The electromagnetic absorber applied to the scatterer is treated as a reflection coefficient at the surface enclosing the scatterer, as in the rightmost illustration in Figure 3. This implies that for each

absorber the reflection coefficient of the planar absorber has to be evaluated for a number of discrete angles of incidence in the range $0 \leq \theta \leq 90°$, both for TE and TM polarization. Further details on how this was carried out are presented in Section 4. Both the presented approximation methods are compared to a corresponding full wave simulation as in the left illustration in Figure 3.

4 Simulation Results - Planar Electromagnetic Absorbers

Three different types of absorbers have been investigated to evaluate the RCS approximation methods introduced in the previous section. The design procedure of the absorbers is presented in detail in [10], where the performance degradation of the absorbers with respect to double curvature was evaluated. The absorbers under study are:

1. A Salisbury absorber, consisting of a resistive sheet with the surface impedance $Z_\mathrm{S} = \eta_0 = 376.7\,\Omega$, located a distance $\lambda_0/4$ from a PEC ground plane.

2. A foam absorber consisting of a conductivity loaded low permittivity material with thickness $9\lambda_0/40$ and relative permittivity $\epsilon_\mathrm{r} = 1 - \mathrm{j}2.39 f_0/f$, coated with a thin dielectric skin with thickness $\lambda_0/40$ and relative permittivity $\epsilon_\mathrm{r} = 4$. The total thickness of the absorber is $\lambda_0/4$. This type of absorber could be realized by utilizing a carbon doped foam [20].

3. A thin magnetic absorber with a thickness of $\lambda_0/20$, relative permeability $\mu_\mathrm{r} = 1 + 1.1/(\mathrm{j}f/f_0 + 0.5)$ and a relative permittivity $\epsilon_\mathrm{r} = 10 + 0.05/(\mathrm{j}f/f_0 + 1)$. This type of absorber could be realized by componds of iron introducing a magnetic dipole moment [20].

The parameter λ_0 is the design wavelength of operation of the absorbers and the geometries can be seen in Figure 4. Simulation results of the three absorbers are presented in Figure 5, where it can be seen that the foam absorber has a wider bandwidth than the other two, but it also a shows larger deviation in performance between TE and TM illumination at oblique angles of incidence.
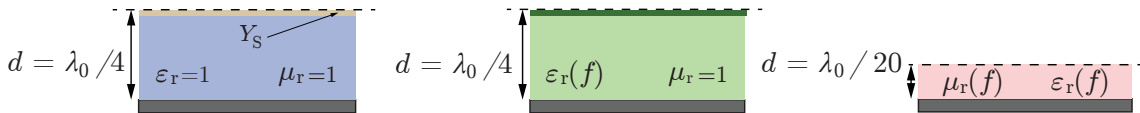

Figure 4: Electromagnetic absorbers used in this work. To the left a Salisbury screen is presented, in the center is a carbon doped foam absorber with a thin dielectric coating, and to the right is a thin magnetic absorber.
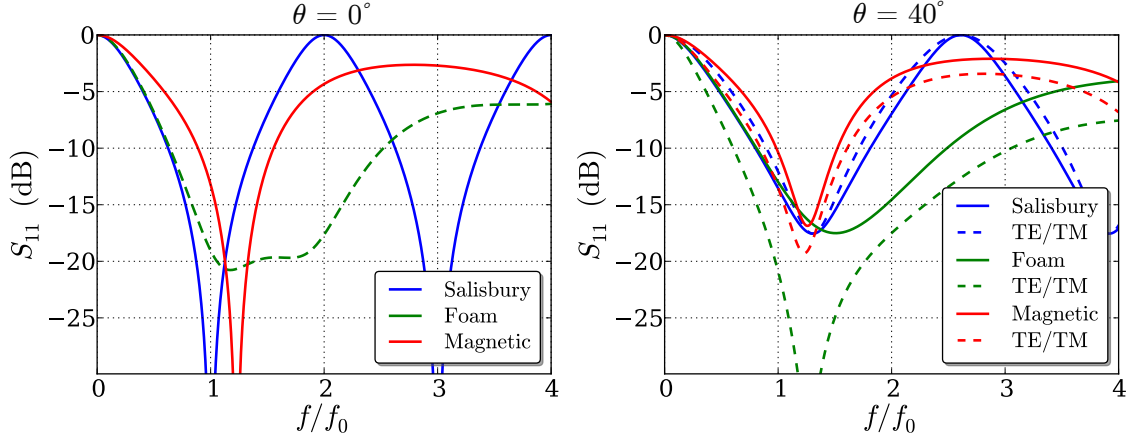
Figure 5: Simulation results of the three absorbers used in this study. To the left, the reflection coefficient of the absorbers are presented ,in dB, for normal incidence. To the right, the reflection coefficient is presented, in dB, for $\theta = 40°$ angle of incidence for TE polarization (solid curves) and TM polarization (dashed curves).

5 Simulation Results - Electromagnetic Absorbers on Axially Symmetric Scatterers

The approximate computation methods for calculating the RCS from axially symmetric scatterers, presented in Section 3, were evaluated for different scatterers with and without different electromagnetic absorbers applied. The RCS of the scatterers under test was determined for on-axis illumination both in a 2D axial symmetric full wave FEM in Comsol Multiphysics, and in an in-house PO solver, written in python using the SciPy package for scientific computing [18]. The electric and magnetic fields were evaluated at 501 frequency points in the range $f_0/200 \leq f \leq 3f_0$ in both solvers, where f_0 is the center frequency of operation of the applied absorbers. Verification simulations and a mesh convergence study of the 2D axial-symmetric full wave solver in Comsol are presented in Appendix C, where simulation results from FEKO are used as a benchmark.

In the full wave model, the maximum mesh size was defined as $\lambda_2/10$, where λ_2 is the wavelength at the highest frequency of the study. In the right illustration in Figure 6 a conical scatterer with a rounded nose and a single layer absorber has been implemented in Comsol Multiphysics. The outer cyan area represent a perfectly matched layer, providing a boundary condition for the numerical solver, the grey area is free space, the rectangle enclosing the scatterer is the line segment γ along which the integral (2.2) is carried out for extracting the monostatic far-field amplitude, and the green area correspond to an electromagnetic absorber coating the scatterer. The structure is illuminated by a plane wave propagating in the upward direction. The simulations were carried out on a Supermicro 2028GR-TR 2U computation server with 2 Intel Xeon E5 8-Core 2.40 GHz processors and 8 Samsung 16GB DDR4 2133MHz RAM. A typical simulation consisted of about 200
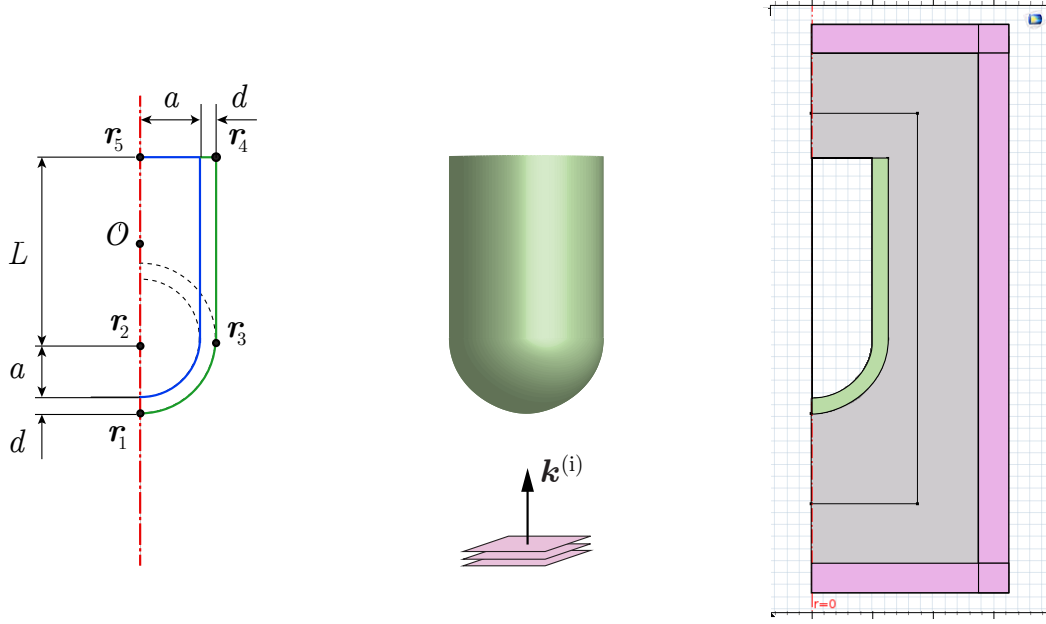
Figure 6: An example of a scattering scenario under test (center), where a scatterer coated with an absorber is illuminated by a plane wave from below the scatterer. Identical simulation models are evaluated in a PO solver (left) and a full wave solver (right). In the PO model the line segment defining the scatterer is parametrized with respect to a predefined coordinate system, and in the full wave model the geometry is generated in a graphical editor.

000–500 000 mesh elements, required about 20-40 GB RAM, and finished in about $12 - 24$ h, depending on the size of the scatterer under study.

In the PO simulations the backscattered far field was determined by evaluation of (2.9) over the line segment defining the surface of the scatterer, using a simple Riemann integral with 10000 elements along the line. Simulations were carried out over the same frequency range as in the full wave software, but this type of approximation method can easily be used for much higher frequencies without a significant increase in computation time. In order to carry out this integral each scatterer under study was parametrized as can be seen in Appendix B. An example of a scatterer under test in this work is presented in the left illustration in Figure 6, where the design parameters of the scatterer are marked and $\boldsymbol{r}_i = (\rho_i, z_i)$, $i = 1, 2, .., 5$ are key points used in the parametrization, see Appendix B for details. A typical PO simulation, evaluating the RCS through the relation (2.9), was carried out in about 5–10 seconds.

In Section 2.2 we mention that the PO far field expression (2.9) will be identically zero for all incidence angles $\theta \leq 0$, resulting in that a PO solver will not catch scattering from the back edge of objects. This type of scattering can be accounted for by utilizing geometrical theory of diffraction (GTD) [14, 19]. However, to compare the two approximation methods in this work the back edge scattering in the full wave simulations is removed by utilizing time gating. This is a well established method

commonly used in electromagnetic measurements to filter out multipath reflections and other unwanted scattering components [9, 11]. By performing a discrete inverse Fourier transform on frequency domain data, multiplying the data with a time domain window function, and finally transforming the data back to the frequency domain, the filtered data is acquired. In order to achieve the desired results, without introducing spurious oscillations in the data, a tapered cosine window function is utilized (commonly referred to as tukey window) [18].

5.1 Hemispherically capped cylinder

The first scatterer under study is a cylinder with a spherical cap, as in Figure 6. The radius of the nose is denoted a and the length of the cylinder L is defined as $L = 3a$, which implies that the total length of the scatterer is $L_{\text{tot}} = 4a$ and the total width is $w_{\text{tot}} = 2a$. Simulation results of a PEC scatterer with $a = 8\lambda_0/3$, are presented in Figure 7. In the top left plot the raw RCS is presented both from a full wave simulation and a PO simulation, where all results are normalized with the gemetrical cross section of the scatterer πa^2. Here it can be seen that the full wave data oscillates rapidly due to the interference of the scattering component from the nose and the back of the scatterer. To compare the two methods the scattering off the back is gated out from the full wave data, and the resulting comparison is made in the upper right plot in Figure 7. Here it can be seen that the agreement between the PO and full wave data is excellent. In the lower left and right plots the full wave and PO data are presented in the time domain, alongside with the tapered cosine window function used to separate the two scattering components. Here it can be seen that the right peak in the full wave data in the lower left plot (corresponding to the back edge scattering) is absent in the PO data in the lower right plot. Still, the same window function is applied to both data sets for consistency. The RCS from the hemispherically capped cylinder coated with the three different absorbers, introduced in Section 4, was evaluated for different sizes of the scatterer. By varying the parameter a the electrical size of the scatterer was varied while keeping the length to width ratio of the PEC scatterer and the thickness of the absorber fixed. Simulation results of the scatterer coated with the foam absorber are presented in Figure 8 and simulation results of the thin magnetic absorber and the Salisbury absorber are presented in Appendix A. Note that the time gating scheme previously described has been utilized in all simulations henceforth presented in this work. In the top left plot in Figure 8, $a = \lambda_0/3$ which corresponds to $L_{\text{tot}} = 4\lambda_0/3$ and $w_{\text{tot}} = 2\lambda_0/3$. In the top right plot $a = 2\lambda_0/3$ which corresponds to $L_{\text{tot}} = 8\lambda_0/3$ and $w_{\text{tot}} = 4\lambda_0/3$. In the lower left plot $a = 4\lambda_0/3$ which corresponds to $L_{\text{tot}} = 16\lambda_0/3$ and $w_{\text{tot}} = 8\lambda_0/3$. Finally, in the lower right plot $a = 16\lambda_0/3$ which corresponds to $L_{\text{tot}} = 64\lambda_0/3$ and $w_{\text{tot}} = 32\lambda_0/3$. Full wave simulation results are marked in red, PO results are marked in blue and results calculated from the first approximation method ($\sigma_{\text{coated}}^{\text{FEM}} \approx \sigma_{\text{PEC}}^{\text{FEM}}|S_{11}^{\text{planar}}|$) are marked in green. Solid curves correspond to simulations of a PEC enclosing the scatterer with absorber coating, denoted with the superscript "PEC". Dashed curves correspond to simulations of the scatterer with the absorber, denoted with the superscript "coated". All results are normalized
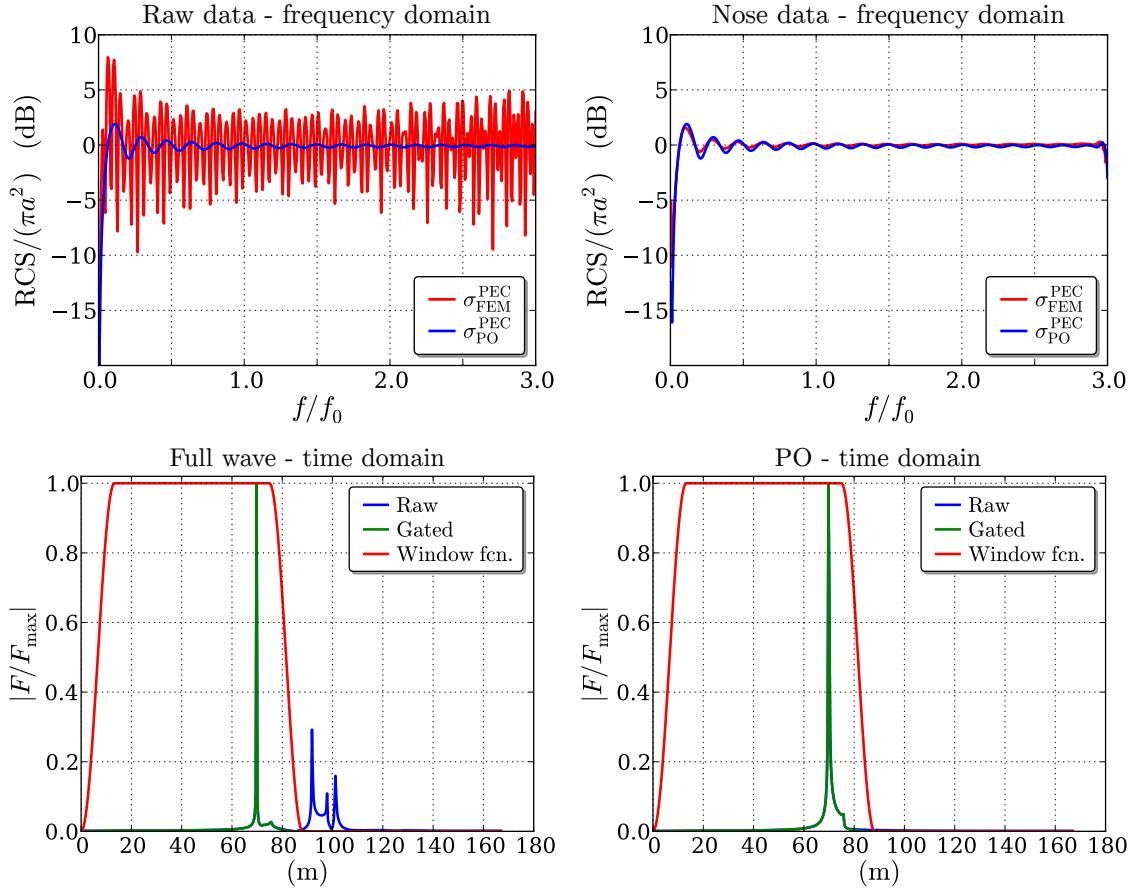
Figure 7: Simulation results of a PEC hemispherically capped cylinder evaluated both in a full wave solver and in a PO solver. The top left plot shows the RCS of the scatterer normalized with its geometrical cross section, presented in the frequency domain. The top right plot shows the normalized RCS when the scattering from the back edge has been gated out in the time domain. The bottom left plot shows the full wave simulation far-field data in the time domain and the bottom right plot is the corresponding PO data, both with the corresponding window function.

with the geometrical cross section of the PEC scatterer without the absorber, *i.e.* $A = \pi a^2$.

In Figure 8 it can be seen that the PEC results from the full wave- and PO simulations agree very well for all sizes of the scatterer. In the case where the scatterer is coated with a foam absorber it can be seen that for the smallest scatterer, in the upper right graph, the approximation methods represented by the blue and green dashed curves deviate from the full wave simulation, represented by the red dashed curve. When the size of the scatterer is increased this deviation is reduced and in the largest case, where the radius of curvature of the scatterer is about $5.3\lambda_0$, the approximation methods yield almost identical results as the full wave simulation.

The same geometry was simulated with a thin magnetic absorber in Figure 15, and with a Salisbury absorber in Figure 16. When comparing the results of the
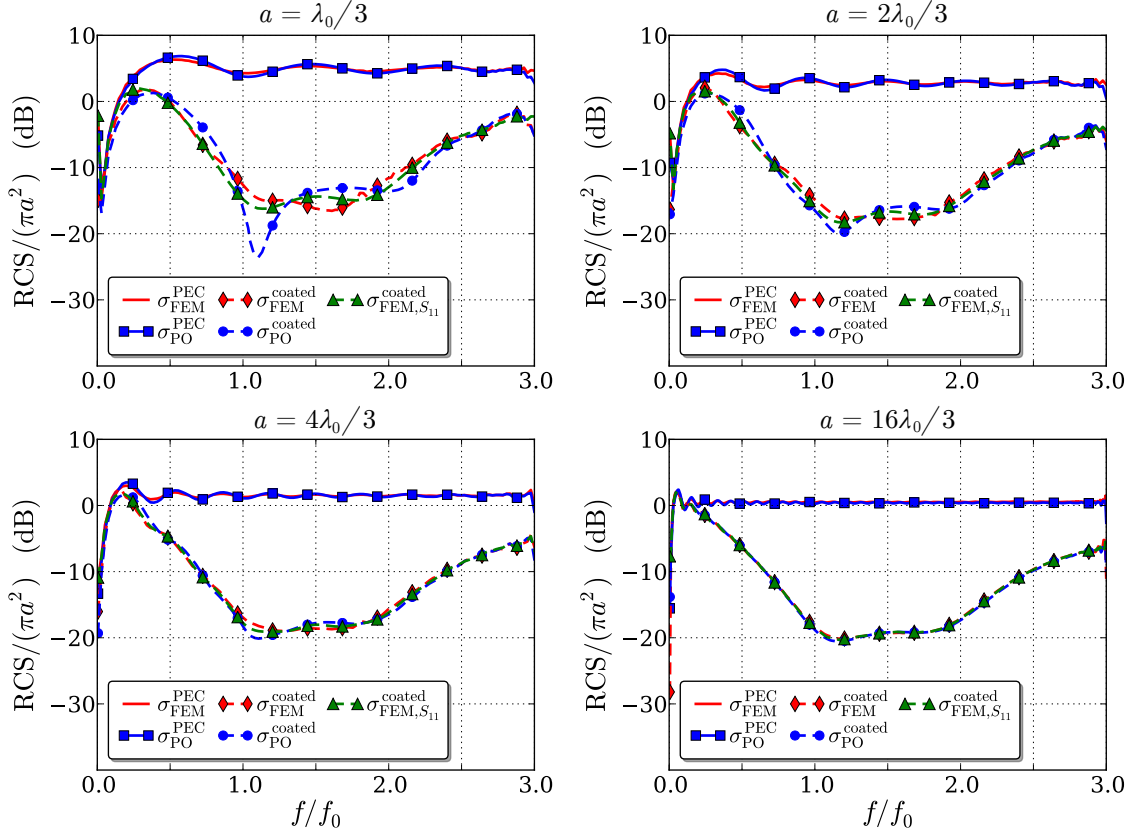
Figure 8: Simulation results of hemispherically capped cylinder scatterers of different sizes, coated with a foam absorber. In the upper left plot the radius of the scatterer is $a = \lambda_0/3$, in the upper right plot $a = 2\lambda_0/3$, in the lower left plot $a = 4\lambda_0/3$, and in the lower right plot $a = 16\lambda_0/3$. The solid curves represent the RCS of a PEC enclosing the coated scatterer and the dashed curves correspond to the RCS of the coated scatterer. The dashed red curve is the full wave simulation, the dashed green curve is the first approximation method and the dashed blue curve is the PO approximation method.

capped cylinder with these three different types of absorbers it can be seen that the accuracy of the RCS approximation methods varies between the different absorbers. The thin magnetic absorber seems to yield the best agreement, closely followed by the foam absorber. The Salisbury absorber also shows good agreement for the larger scatterers, but relatively poor agreement for radii of curvature $\lesssim 2\lambda_0$. This effect was investigated in great detail in [10], where it was concluded that absorbers based on "volume losses" such as in foam absorbers or thin magnetic absorbers are less sensitive to curvature than absorbers based on single or multiple layers of thin resistive sheets. Both approximation methods used in this work assume "local flatness" and this approximation is thus valid for smaller radii of curvature for absorbers that utilize volume losses.

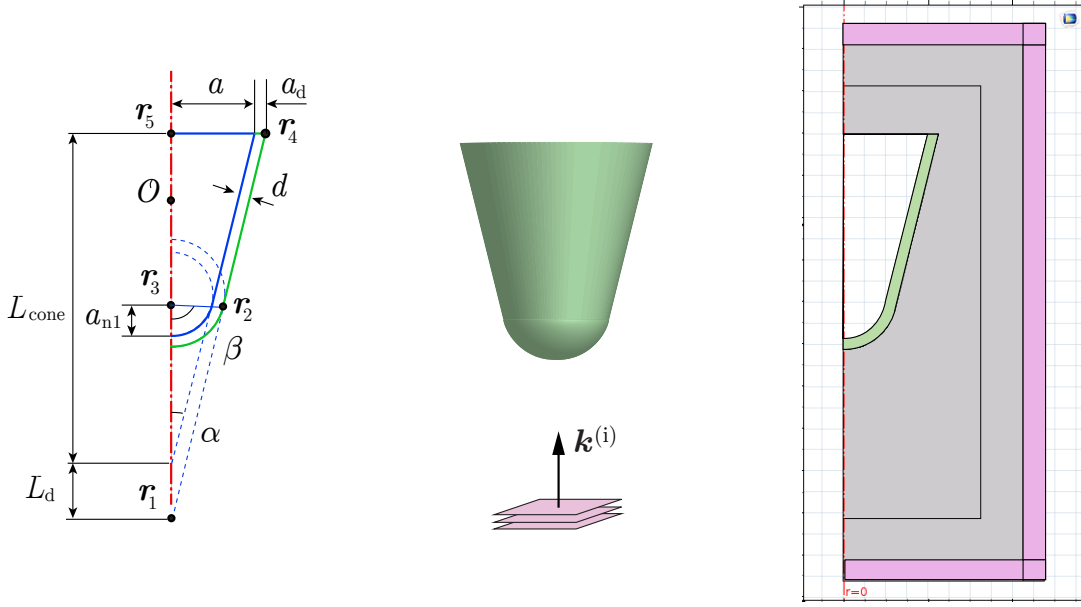Figure 9: An example of a scattering scenario under test (center), where a scatterer coated with an absorber is illuminated by a plane wave from below the scatterer. Identical simulation models are evaluated in a PO solver (left) and a full wave solver (right). In the PO model the line segment defining the scatterer is parametrized with respect to a predefined coordinate system, and in the full wave model the geometry is generated in a graphical editor.

5.2 Rounded cone

The next geometry under test is a cone with a rounded nose, as in the middle illustration in Figure 9. To the left in Figure 9 the PO geometry of the cone is presented and to the right is the corresponding full wave simulation model in Comsol. The radius of curvature of the nose of the scatterer is denoted a_{n1}, and the length to width ratio of the cone is the same as for the capped cylinder in Figure 6 resulting in the cone half angle $\alpha = \tan^{-1}(1/4) \approx 14°$. The angle defining the intersection between the spherical nose and the straight cone segment β is calculated as a function of a_{n1} tp achieve a smooth transition. The scattering contribution from the back edge of the scatterer is gated out in all simulations of this geometry.

This geometry is of interest for evaluating the accuracy of the RCS approximation methods for radii of curvature smaller than λ_0. A general rule of thumb for achieving high accuracy using a PO solver is to avoid simulating geometries with radii of curvature smaller than a few wavelengths in size, which indicates that we might see deviations between full wave simulations and the approximation methods. The length and width of the underlying cone are now fixed as $w = 4\lambda_0$, $L_{tot} = 8\lambda_0$ while the radius of curvature of the nose is varied $a_{n1} = [\lambda_0/20, \lambda_0/4, \lambda_0/2, 3\lambda_0/4]$, see Figure 10. The results in Figure 11 show simulations of the rounded cone scatterer with the nose radius increasing from the upper right to the lower left graph. Here

Figure 10: Cone scatterers with a spherically rounded nose. The radius of curvature of the PEC scatterers, denoted $a_{\mathrm{n}1}$, is increasing from left to right.

Figure 11: Simulation results of rounded cone scatterers of the same underlying size and with a varying radius of curvature in the nose, coated with a foam absorber. In the upper left plot the radius of the nose of the scatterer is $a_{\mathrm{n}1} = \lambda_0/20$, in the upper right plot $a_{\mathrm{n}1} = \lambda_0/4$, in the lower left plot $a_{\mathrm{n}1} = \lambda_0/2$, and in the lower right plot $a_{\mathrm{n}1} = 3\lambda_0/4$. The solid curves represent the RCS of a PEC enclosing the coated scatterer and the dashed curves correspond to the RCS of the coated scatterer. The dashed red curve is the full wave simulation, the dashed green curve is the first approximation method and the dashed blue curve is the PO approximation method.

it can be seen that for a radius of curvature on the order of $\lambda_0/2$ the RCS from the approximation methods and the full wave simulations deviate, but for a_{n1} in the lower right plot in Figure 11 the approximation methods yield accurate results.

In the same manner as for the previous geometry, the rounded cone scatterer was simulated with a thin magnetic absorber and a Salisbury absorber, for different radii of curvature of the nose, and the results are presented in Figures 17, 18. When comparing the results of the different absorbers a similar behavior is observed as for the capped cylinder, *i.e.* that the agreement of the approximation methods and the full wave simulations is best for the thin magnetic absorber, slightly worse for the foam absorber and noticeably less accurate for the Salisbury absorber. In the magnetic absorber case the agreement is very good already at $a_{\mathrm{n1}} = \lambda_0/4$. A peculiar behavior is observed in the Salisbury results, where in the PO simulations the absorber actually imply a larger RCS than the uncoated scatterer. This is most likely a result of the uncertainty of the method, and it can be seen that this effect is reduced as the radius of curvature of the scatterer is increased. It can also be seen that the agreement between the PO simulations and the full wave simulations of the uncoated scatterer is excellent for all cases evaluated, even when the radius of curvature is $\ll \lambda$.

In Appendix A.4, simulation results are presented for a sharp cone tip, with and without a Salisbury absorber. As in the previous simulated cases, the scattering from the back edge of the structure has been removed by using time gating. In Figure 21 it can be seen that the agreement between PO and full wave simulations is good for a PEC scatterer. However, it can also be seen that the proposed approximation method, using the PO solver, is not at all accurate when the cone tip is coated with an absorber. This is expected since the PO uses the interaction of the incident signal with the PEc cone and the absorber is more complicated than what can be modeled with a local reflection coefficient on a planar surface.

5.3 Rounded cone-cylinder

The final geometry under study in this work is a combination of the scatterers in Sections 5.1-5.2. A cone with a spherically rounded nose and a cylinder are merged, and a rounding of the same radius of curvature as at the nose is introduced at the joint. In Figure 12 an example of the scatterer is presented in the center illustration, and the corresponding simulation model implemented in Comsol and in the PO solver are presented to the right and left, respectively. The half angle of the cone segment is given by $\alpha \approx 14°$, as was the case in the rounded cone scatterer in the previous section. The size of the scatterer was defined as $w = 8\lambda_0/3$, $L_{\mathrm{tot}} = 32\lambda_0/3$ to avoid very long simulation times when generating the full wave simulation results. Just as for the previous geometries the scattering from the back edge of the cylinder is gated out.

A parametric sweep was carried out were the radius of curvature of the nose and the rounded joint was varied as $A_{\mathrm{n1}} = [\lambda_0/10, \lambda_0/4, \lambda_0/2, \lambda_0, 4\lambda_0/3]$. When the radius of curvature of the nose and joint take the value of half the width of the scatterer, as in the rightmost illustration in Figure 13, the center of the two spher-
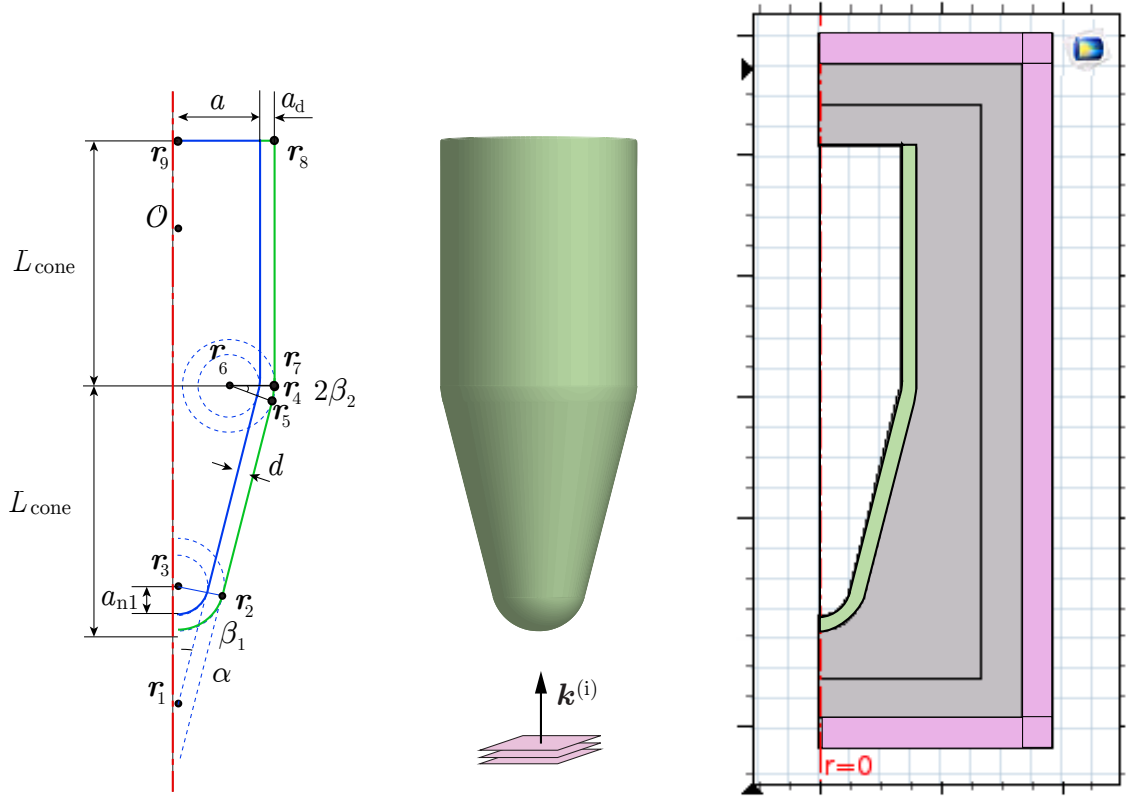
Figure 12: An example of a scattering scenario under test (center), where a scatterer coated with an absorber is illuminated by a plane wave from below the scatterer. Identical simulation models are evaluated in a PO solver (left) and a full wave solver (right).
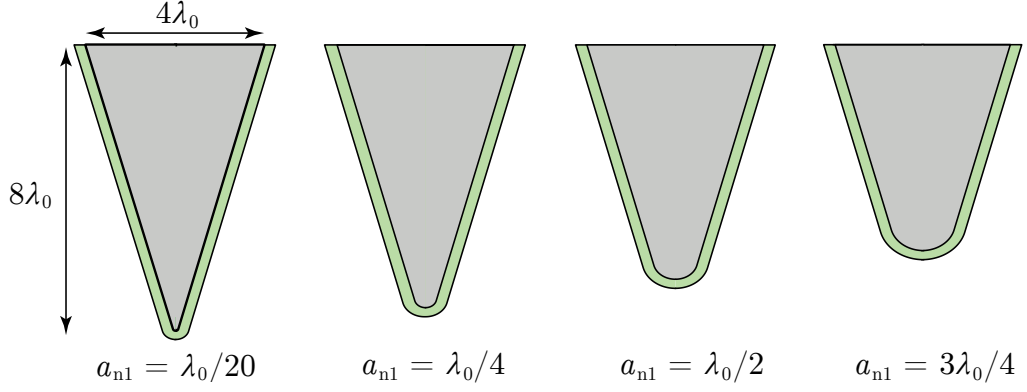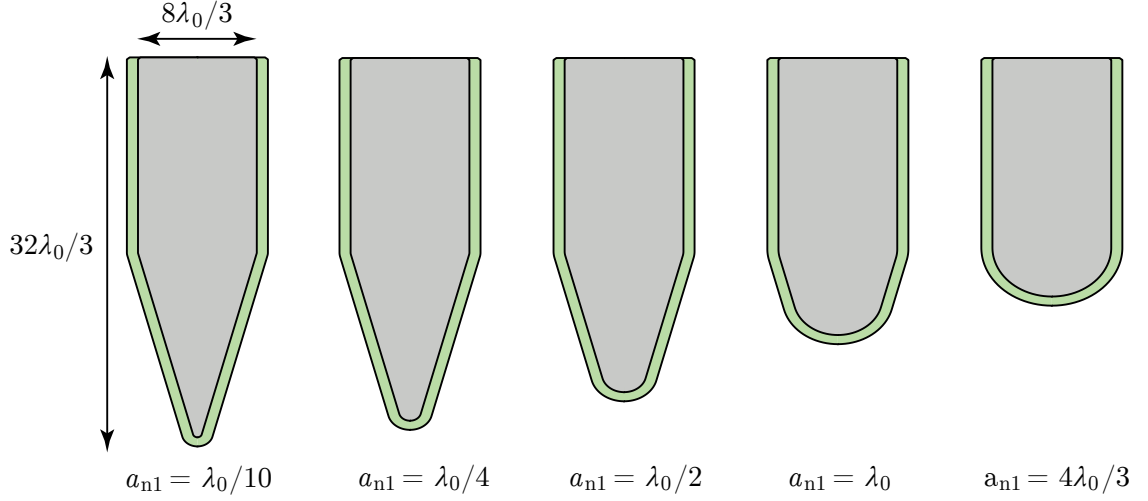

Figure 13: Cone-cylinder scatterers with a spherically rounded nose and middle edge. The radius of curvature of the PEC scatterers, denoted a_{n1}, is increasing from left to right.
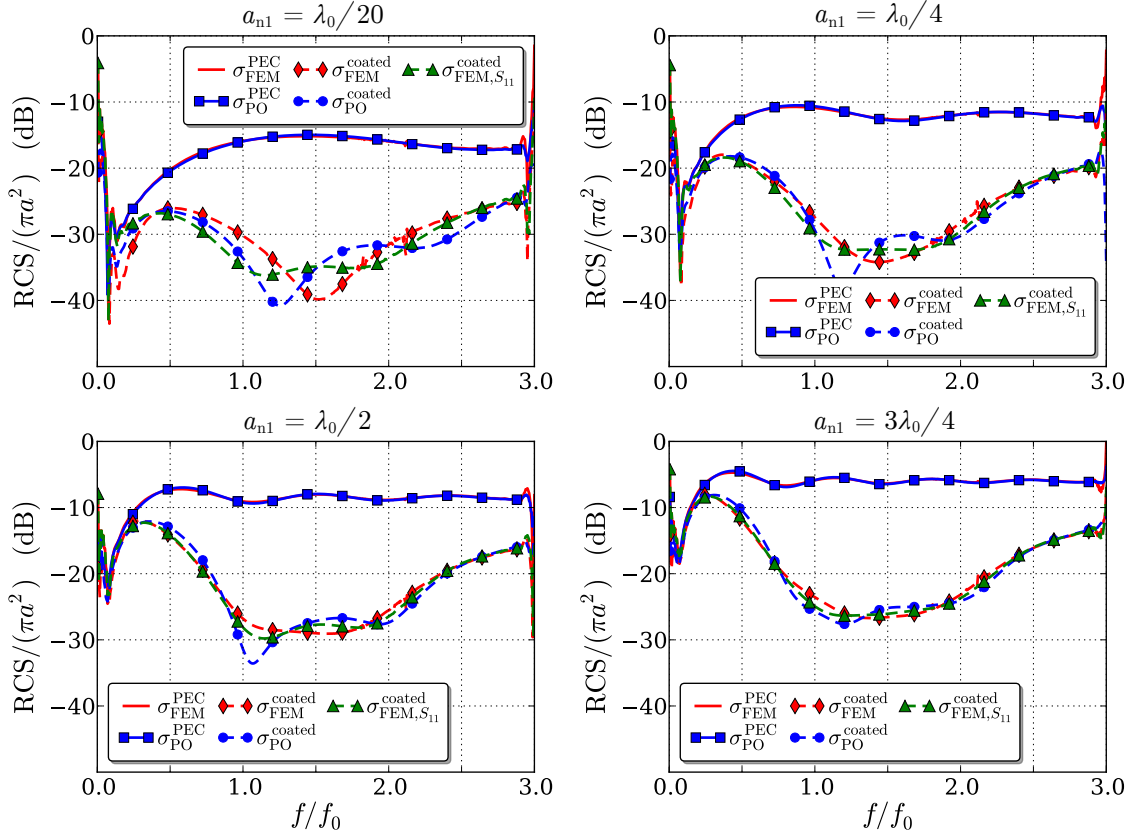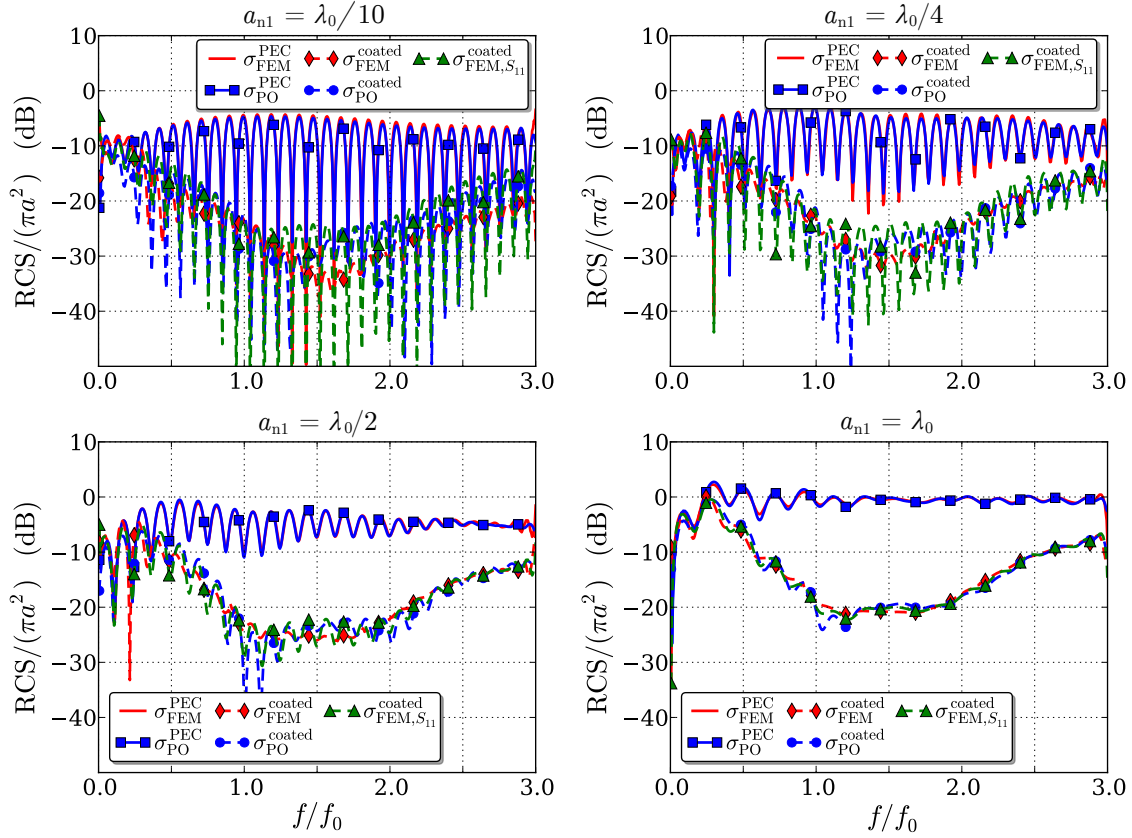
Figure 14: Simulation results of rounded cone-cylinder scatterers of the same underlying size and with a varying radius of curvature in the nose, coated with a foam absorber. In the upper left plot the radius of the nose of the scatterer is $a_{n1} = \lambda_0/10$, in the upper right plot $a_{n1} = \lambda_0/4$, in the lower left plot $a_{n1} = \lambda_0/2$, and in the lower right plot $a_{n1} = \lambda_0$. The solid curves represent the RCS of a PEC enclosing the coated scatterer and the dashed curves correspond to the RCS of the coated scatterer. The dashed red curve is the full wave simulation, the dashed green curve is the first approximation method and the dashed blue curve is the PO approximation method.

ical components coincide and structure takes the same form as the hemispherically capped cylinder in Section 5.1. The results of this scenario is presented for the three different absorbers in the lower left plot in Figure 8 and Figures 15–16.

Simulation results of the rounded cone-cylinder are presented in Figure 14, where the radius of curvature of the nose is increased in the order from the upper left plot, to the upper right, to the lower left and finally the lower right plot. For the smallest nose curvature in the upper left plot all curves are oscillating quite rapidly due to interference between the signals scattered from the nose and the joint between the cone and the cylinder parts of the scatterer. It can be seen that the agreement between PO- and full wave simulations is still very good in the PEC scenario, but in the absorber case the approximation methods are showing much larger oscillations

than the full wave simulations. As the radius of curvature of the nose is increased the oscillations of the absorber coated curves are reduced and the approximation methods yield better results. When comparing the results in Figure 14 with the results of the rounded cone in Figure 11 it is observed that the approximation methods yield better results for the cone scatterer. This is most likely due to the fact that both methods are based on a "local flatness" assumption, which is very accurate for specular reflections, but not as accurate for non-specular (or diffused) reflections. The second type of reflections are often a result on diffraction, which is not fully incorporated in PO.

The geometries in Figure 13 were also evaluated for the thin magnetic absorber and the Salisbury absorber and the results are presented in Figures 19–20. Here it can be seen that the approximation methods yield similar accuracy for the foam absorber and the magnetic absorber, where reasonably accuracy is achieved when $a_{n1} \geq \lambda_0/2$. For the Salisbury absorber the accuracy is significantly worse and good agreement is not achieved in any of the scenarios evaluated.

6 Evaluation of Approximation Methods

The two approximation methods introduced in this work have been thoroughly evaluated and it has been shown that in most cases they yield similar results. this is most likely due to the fact that the PO- and full wave simulations of a PEC enclosing the scatterer show excellent agreement for all geometries evaluated, as long as the diffraction scattering from the back edge is gated out. The first method is relatively fast if simulated in a full wave solver, since the absorber is not meshed in the simulation model. However, if a PO solver is used, as in the second approximation method, the simulations are carried out in a few seconds since only a line integral describing the scatterer is required.

It has been shown that for specular reflections the approximation methods yield accurate results for scatterers coated with an absorber, when the radius of curvature of the scatterer is larger that about $\lambda_0/2 - \lambda_0$. But it has also been observed that both methods yield significantly better agreement for the foam absorber and the magnetic absorber than the Salisbury absorber. This behavior was described in detail for spherical scatterers in [10], where it was concluded that absorbers based on single or multiple layers of resistive sheets are more sensitive to curvature than absorbers based on "volume losses". Since the approximation methods used in this work are derived from the work in [10] it was expected that the same behavior is observed for the scatterers under study. The agreement between the approximation methods and the full wave simulations was not as good for the final geometry under study as for the previous two geometries. This is most likely due to the fact that the scattering from the joint between the cylinder and the cone components of the scatterer is causing non-specular reflections that are not as accurately modeled by PO as ordinary specular reflections.

7 Conclusions

Two approximation methods have been presented for calculating monostatic RCS from axial-symmetric scatterers coated with electromagnetic absorbers. The methods are designed for plane wave illumination parallel to the axis of rotation of the scatterer. The first methods is based on simulating the scattering of a PEC enclosing the absorber coated scatterer, and multiplying the result with the squared magnitude of the absorber reflection coefficient in a planar scenario. The second method is based on simulating the scattering scenario in a PO solver, where the electromagnetic absorber is treated as a reflection dyadic at the outer surface of the scatterer. Both methods result in a significant acceleration in computation speed, where the PO method carries out the computations in a number of seconds.

The monostatic scattering from three different geometries have been investigated, and parametric sweeps were carried out to test the limits where the methods yield accurate results. The two methods yield similar results in most cases evaluated in this study. This is due to the fact that the agreement between PO- and full wave simulations of a PEC scatterer is excellent, even for radii of curvature much smaller that the wavelength of incident signals. For specular reflections, the approximation methods yield very accurate results compared to full wave simulations when the radius of curvature is on the order of 1/2-1 wavelength of the signal. It is also concluded that the accuracy of the two methods vary depending on what type of absorber is applied to the scatterer, and that absorbers based on "volume losses" such as carbon doped foam absorber and thin magnetic absorbers yield better results than for absorbers based on resistive sheets, such as a Salisbury absorber.

A   Simulation Results

In this appendix, a collection of simulation results are presented. All geometries introduced in Section 5 have been coated with a thin magnetic absorber or a Salisbury absorber, defined in Section 4, and the monostatic scattering results are presented in Figures 15-20. In Section A.4, simulation results are presented for a sharp cone tip, with and without an absorber.

A.1   Hemispherically capped cylinder

A.1.1   Thin magnetic absorber
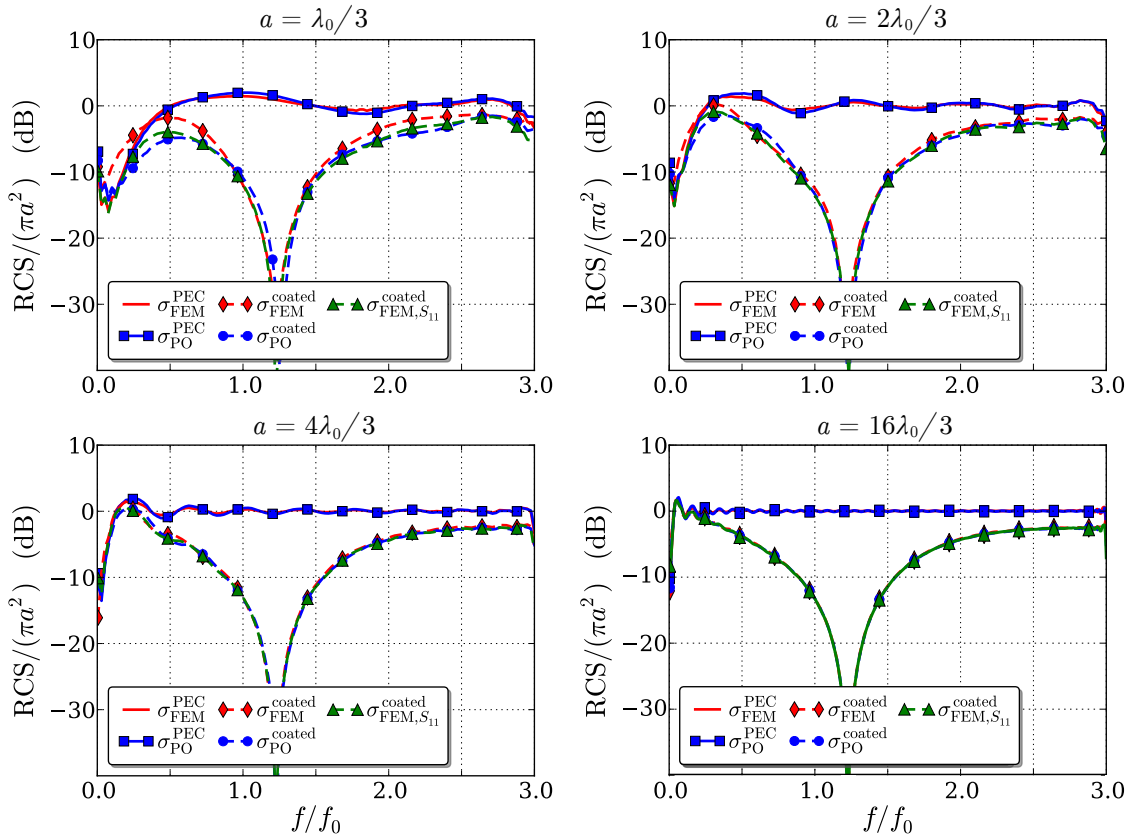
Figure 15: Simulation results of capped cylinder scatterers of different sizes, coated with a thin magnetic absorber. In the upper left plot the radius of the scatterer is $a = \lambda_0/3$, in the upper right plot $a = 2\lambda_0/3$, in the lower left plot $a = 4\lambda_0/3$, and in the lower right plot $a = 16\lambda_0/3$. The solid curves represent the RCS of a PEC enclosing the coated scatterer and the dashed curves correspond to the RCS of the coated scatterer. The dashed red curve is the full wave simulation, the dashed green curve is the first approximation method and the dashed blue curve is the PO approximation method.

A.1.2 Salisbury absorber

Figure 16: Simulation results of capped cylinder scatterers of different sizes, coated with a Salisbury absorber. In the upper left plot the radius of the scatterer is $a = \lambda_0/3$, in the upper right plot $a = 2\lambda_0/3$, in the lower left plot $a = 4\lambda_0/3$, and in the lower right plot $a = 16\lambda_0/3$. The solid curves represent the RCS of a PEC enclosing the coated scatterer and the dashed curves correspond to the RCS of the coated scatterer. The dashed red curve is the full wave simulation, the dashed green curve is the first approximation method and the dashed blue curve is the PO approximation method.

A.2   Rounded cone

A.2.1   Thin magnetic absorber

Figure 17: Simulation results of rounded cone scatterers of the same underlying size and with a varying radius of curvature in the nose, coated with a thin magnetic absorber. In the upper left plot the radius of the nose of the scatterer is $a_{n1} = \lambda_0/20$, in the upper right plot $a_{n1} = \lambda_0/4$, in the lower left plot $a_{n1} = \lambda_0/2$, and in the lower right plot $a_{n1} = 3\lambda_0/4$. The solid curves represent the RCS of a PEC enclosing the coated scatterer and the dashed curves correspond to the RCS of the coated scatterer. The dashed red curve is the full wave simulation, the dashed green curve is the first approximation method and the dashed blue curve is the PO approximation method.

A.2.2 Salisbury absorber

Figure 18: Simulation results of rounded cone scatterers of the same underlying size and with a varying radius of curvature in the nose, coated with a Salisbury absorber. In the upper left plot the radius of the nose of the scatterer is $a_{n1} = \lambda_0/20$, in the upper right plot $a_{n1} = \lambda_0/4$, in the lower left plot $a_{n1} = \lambda_0/2$, and in the lower right plot $a_{n1} = 3\lambda_0/4$. The solid curves represent the RCS of a PEC enclosing the coated scatterer and the dashed curves correspond to the RCS of the coated scatterer. The dashed red curve is the full wave simulation, the dashed green curve is the first approximation method and the dashed blue curve is the PO approximation method.

A.3   Rounded cone-cylinder

A.3.1   Magnetic absorber
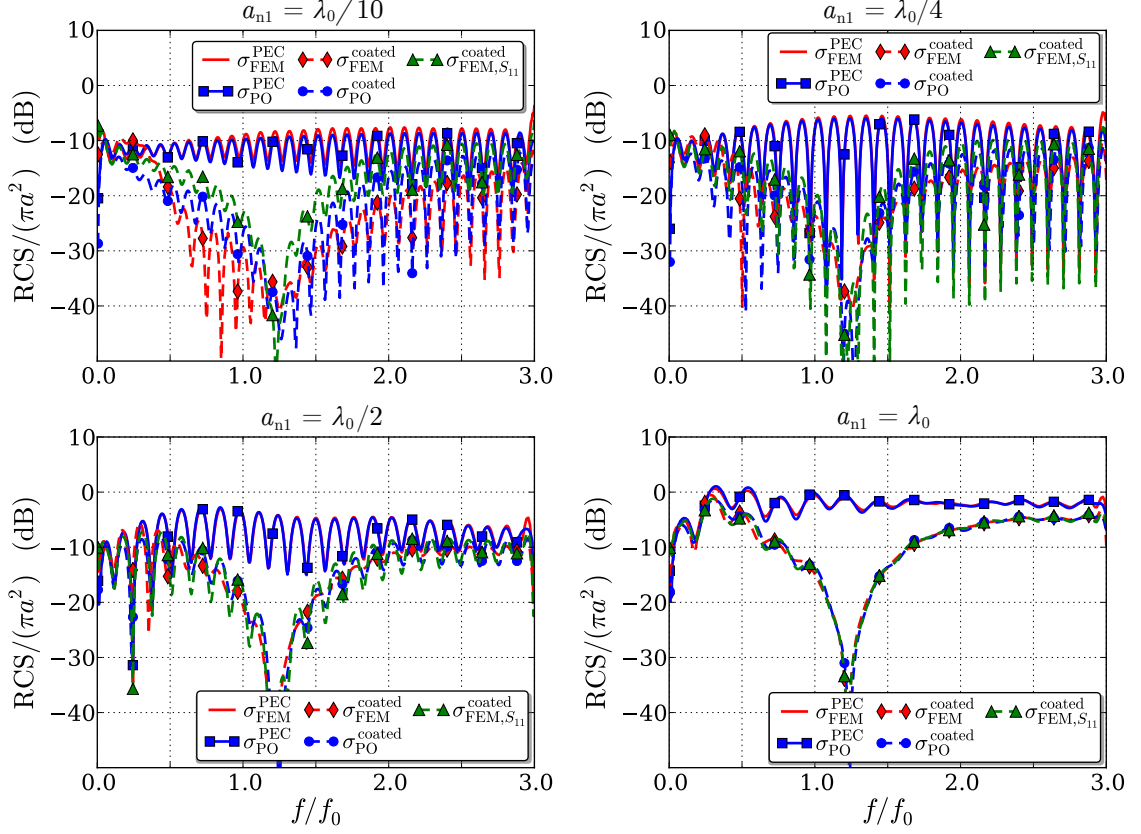
Figure 19: Simulation results of rounded cone-cylinder scatterers of the same underlying size and with a varying radius of curvature in the nose, coated with a thin magnetic absorber. In the upper left plot the radius of the nose of the scatterer is $a_{n1} = \lambda_0/10$, in the upper right plot $a_{n1} = \lambda_0/4$, in the lower left plot $a_{n1} = \lambda_0/2$, and in the lower right plot $a_{n1} = \lambda_0$. The solid curves represent the RCS of a PEC enclosing the coated scatterer and the dashed curves correspond to the RCS of the coated scatterer. The dashed red curve is the full wave simulation, the dashed green curve is the first approximation method and the dashed blue curve is the PO approximation method.
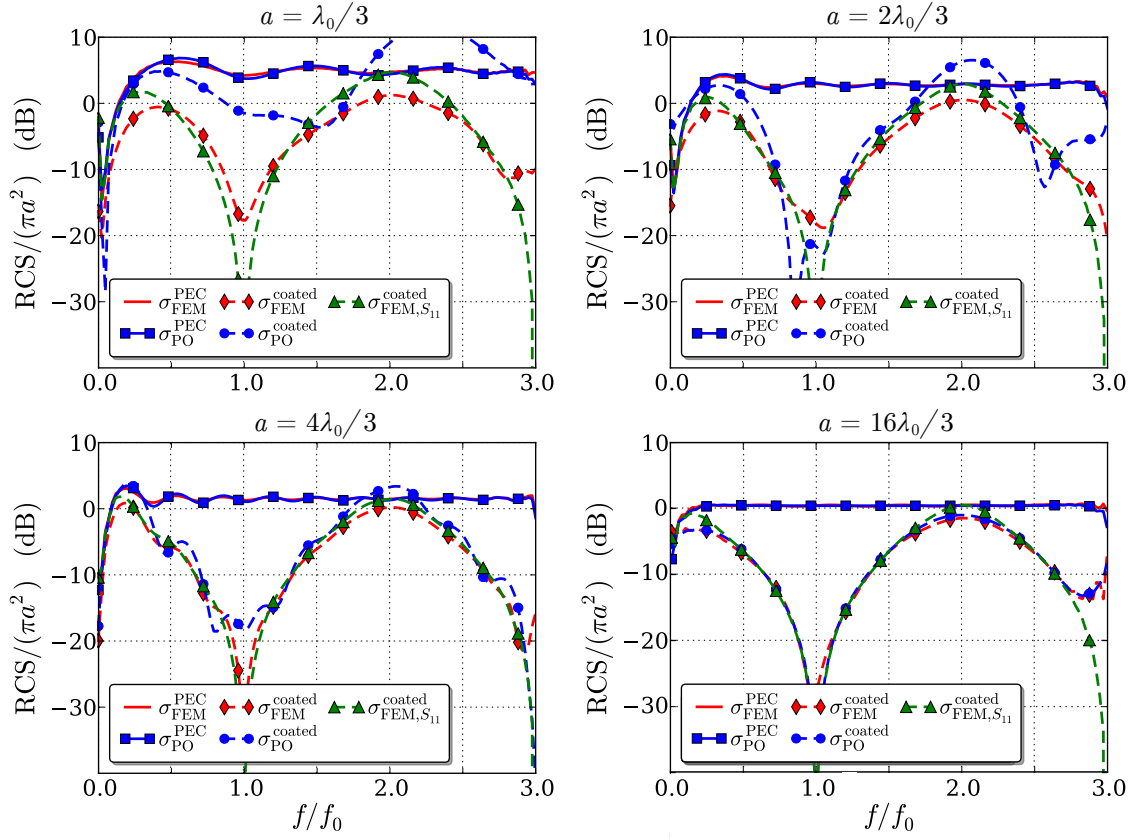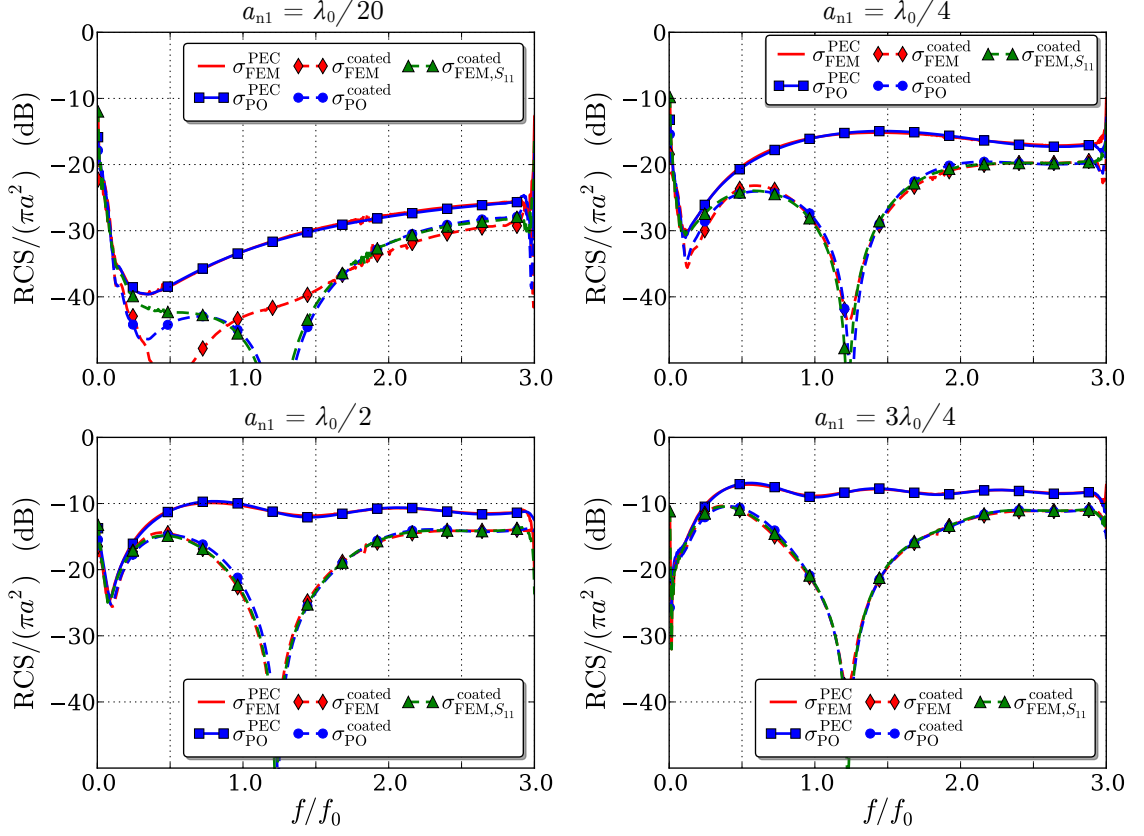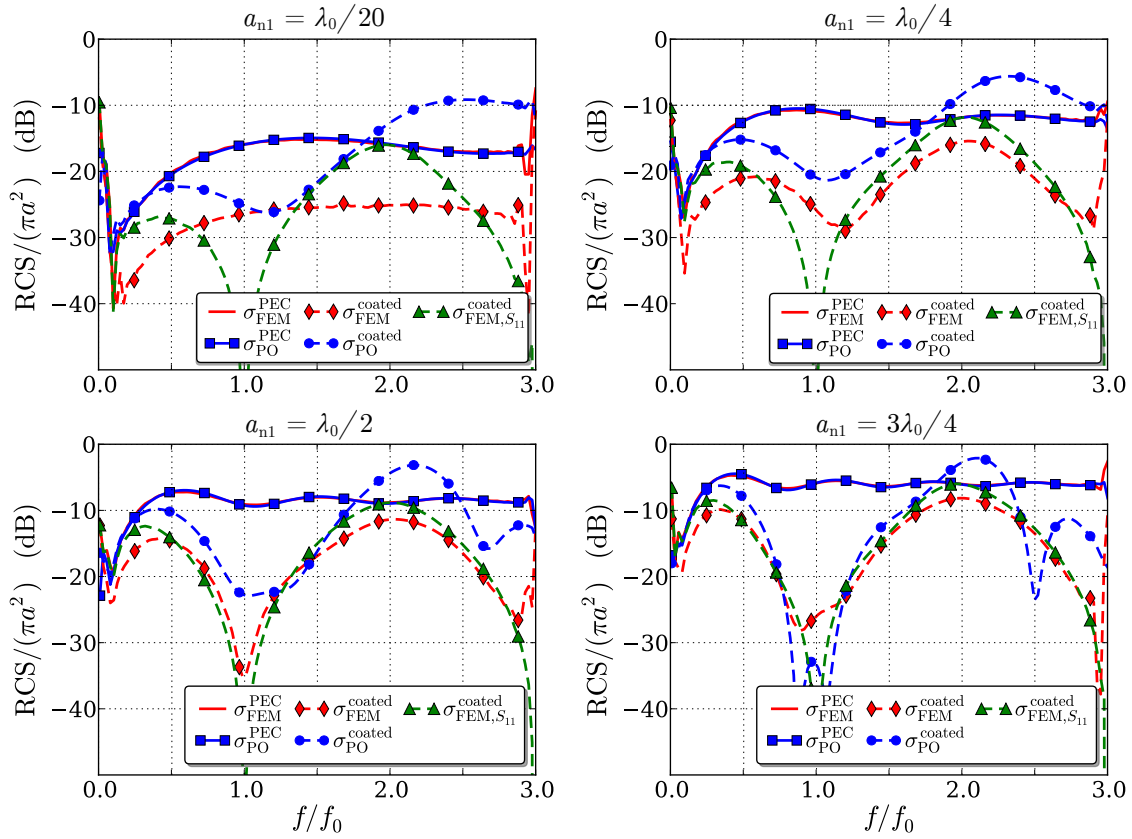
A.3.2   Salisbury absorber
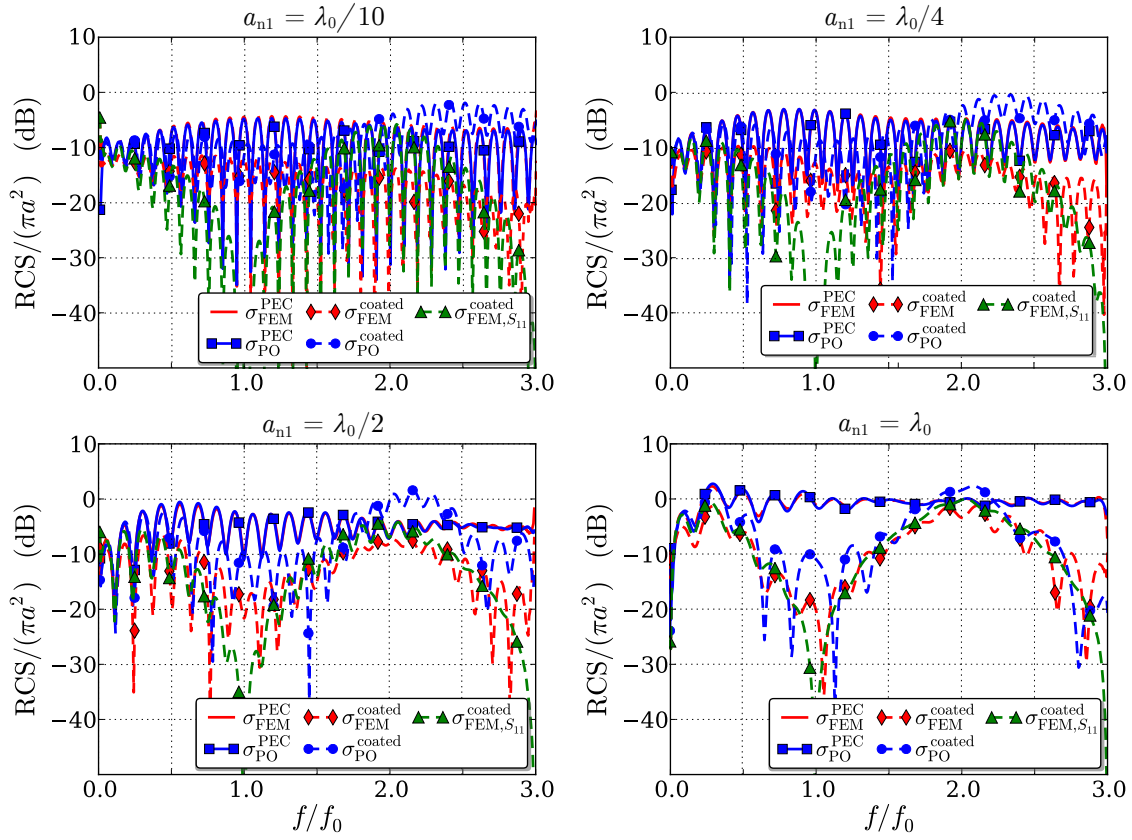
Figure 20: Simulation results of rounded cone-cylinder scatterers of the same underlying size and with a varying radius of curvature in the nose, coated with a Salisbury absorber. In the upper left plot the radius of the nose of the scatterer is $a_{\mathrm{n1}} = \lambda_0/10$, in the upper right plot $a_{\mathrm{n1}} = \lambda_0/4$, in the lower left plot $a_{\mathrm{n1}} = \lambda_0/2$, and in the lower right plot $a_{\mathrm{n1}} = \lambda_0$. The solid curves represent the RCS of a PEC enclosing the coated scatterer and the dashed curves correspond to the RCS of the coated scatterer. The dashed red curve is the full wave simulation, the dashed green curve is the first approximation method and the dashed blue curve is the PO approximation method.

A.4   Sharp cone tip

For the sake of completeness, the scattering from a sharp cone tip was simulated, both using a full wave solver and the in-house code. The geometry of the scatterer can be seen in B.3, the size of the scatterer was defined as $a = 4\lambda_0/3$, and the same frequency range was used as in previous simulations. In [20, p.255], the monostatic scattering from a cone tip is stated to be approximately related to the opening angle
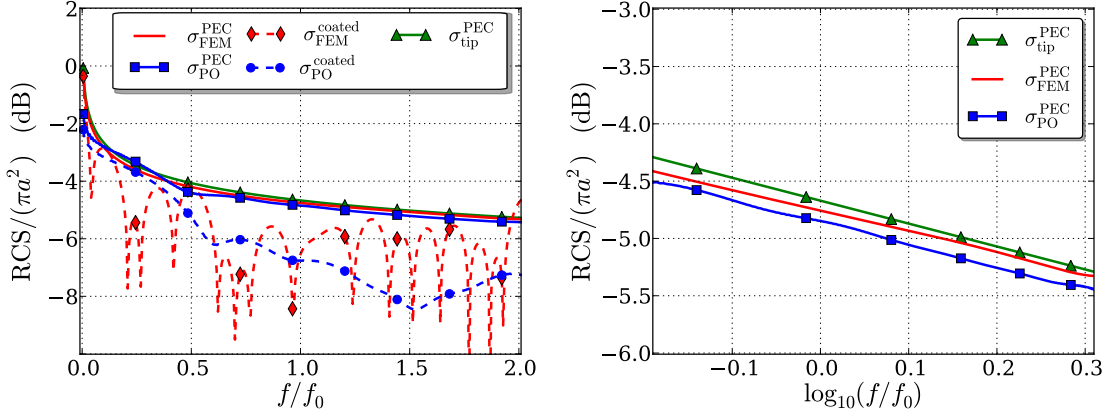
Figure 21: Simulation results of a PEC cone tip, with and without a foam absorber applied. To the left, simulation results from the in-house PO solver and a full wave solver are compared to the asymptotic scattering from a cone tip in (A.1). To the right, the PO scattering data is plotted in log-log scale and the simulated results are compared to the asymptotic relation.

of the cone 2α, and the frequency f as

$$\sigma_{\text{tip}}^{\text{PEC}} \approx (0.256 \cdot 2\alpha)^{4.3} \left(\frac{c_0}{f} \right)^2. \tag{A.1}$$

This result is verified in Figure 21 where simulation results are presented for the scattering from a cone tip. In order to evaluate if the approximation method based on PO simulations is accurate in this type of scenario, a foam absorber was also added to the structure, seâĂŹ the dashed lines in Figure 21. The scattering data from the cone is truncated using time gating, but to extract the desired information a small modification is applied to the time gating procedure. Due to the frequency dependency of the cone tip scattering contribution (A.1), the spectrum of the scattered far field was weighted before transformation into the time domain. The spectrum of a derivated Gaussian pulse was here used as a weighting function. This weight function, operating on the scattered far field, have a linear frequency slope which was used to compensate for the $1/f^2$-dependency in the RCS of (A.1). Without this operation, it is not possible to separate the scattered contributions from the cone tip and the rest of the structure the in time domain. This weighting operation was compensated for after the signal had been gated and transformed back to the frequency domain.

   In the left plot in Figure 21, simulation results are compared to the asymptotic relation (A.1) and it can be seen that the PO and full wave simulation results agree very well with the asymptotic relation. In the case with a foam absorber applied it can be seen that the approximative results acquired using PO deviate from the full wave simulation results. This indicates that the proposed approximation methods is not suitable for calculating scattering from sharp edges coated with an electromagnetic absorber. In the right plot in Figure 21, the scattering from a PEC

cone tip is calculated using FEM, PO and the expression (A.1) and plotted in log-log scale. Here it can be seen that the slope of the three curves, corresponding to the frequency dependency of $1/f^2$ is almost identical in the three curves. The slight vertical shift that can be seen is most likely caused by the gating procedure.

B Parametrization of Axially Symmetric Objects

A detailed parametrization of each scatterer under study is presented in this appendix.

B.1 General theory

A curve γ defining a axially symmetric scatterer can be parametrized by a real scalar q:

$$\gamma = \{\boldsymbol{r}(q) : \ 0 \leq q \leq 1\}, \tag{B.1}$$

where $\boldsymbol{r}(q) = \rho(q)\hat{\boldsymbol{\rho}} + z(q)\hat{\boldsymbol{z}}$. The start point $\boldsymbol{r}(0)$ is chosen at the bottom of each scatterer and the end point $\boldsymbol{r}(1)$ is at the top. Defining the unit vector as

$$\hat{\boldsymbol{n}}(q) = \frac{z'(q)\hat{\boldsymbol{\rho}} - \rho'(q)\hat{\boldsymbol{z}}}{\sqrt{(z'(q))^2 + (\rho'(q))^2}} \tag{B.2}$$

then makes it point out of the object (in the typical case, we have $z'(q) \geq 0$). The angle of incidence is given by

$$\cos\theta = -\hat{\boldsymbol{z}} \cdot \hat{\boldsymbol{n}}(q) = \frac{\rho'(q)}{\sqrt{(z'(q))^2 + (\rho'(q))^2}}. \tag{B.3}$$

Finally, the length element is $\mathrm{d}\ell = (\mathrm{d}\ell/\mathrm{d}q)\,\mathrm{d}q$, where

$$\frac{\mathrm{d}\ell}{\mathrm{d}q} = \sqrt{(z'(q))^2 + (\rho'(q))^2}. \tag{B.4}$$

In special cases it may be easier to do the parametrization more explicitly. The approach that is used here is to identify the location of key points of the geometry in a global coordinate system $\boldsymbol{r}_i = (\rho_i, z_i)$, break down the parametrization in separate regions, and from these points determine the parametrization of the scatterer.

B.2 Hemispherically capped cylinder

To parametrize a hemispherically capped cylinder coated with an absorber as in Figure 22 the parametrization is broken down to three regions. Key points of the geometry are identified and marked in Figure 22, and the coordinates of these points are defined in Table 1 where L is the length of the cylinder, a is the radius of the hemispherical nose and $a_{\mathrm{n}} = a + d$ is the radius of the absorber coated hemispherical nose. Here, it is clearly seen that the straight part of the cylinder and the flat top do not satisfy $\cos\theta > 0$, and hence are in the shadow region in the physical optics approximation.
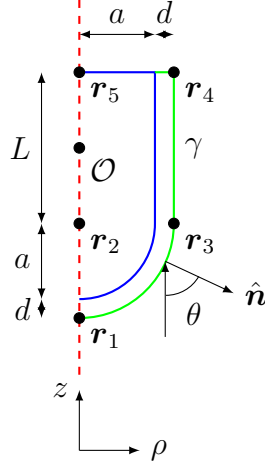
Figure 22: A typical geometry, with a hemispherically capped right circular cylinder of height L and radius a. The total height is $L + a$.

Table 1: Key points of interest for parametrization of a hemispherically capped cylinder coated with an absorber.

	$\boldsymbol{r}_1$	$\boldsymbol{r}_2$	$\boldsymbol{r}_3$	$\boldsymbol{r}_4$	$\boldsymbol{r}_5$
ρ_i	0	0	a_{n}	a_{n}	0
z_i	$-L/2 - a_{\mathrm{n}}$	$-L/2$	$-L/2$	$L/2$	$L/2$

Table 2: Parametrization of hemispherically capped cylinder coated with an absorber.

	Spherical nose	Straight cylinder	Flat top
q	$0 \leq q < 1/3$	$1/3 \leq q < 2/3$	$2/3 \leq q \leq 1$
$\rho(q)$	$a_{\mathrm{n}} \sin(q3\pi/2)$	ρ_3	$\rho_4 - \rho_4(3q - 2)$
$z(q)$	$z_2 - a_{\mathrm{n}} \cos(q3\pi/2)$	$z_3 + (z_4 - z_3)(3q - 1)$	z_5
$\hat{\boldsymbol{n}}(q)$	$\sin(q3\pi/2)\hat{\boldsymbol{\rho}} - \cos(q3\pi/2)\hat{\boldsymbol{z}}$	$\hat{\boldsymbol{\rho}}$	$\hat{\boldsymbol{z}}$
$\mathrm{d}\ell/\mathrm{d}q$	$|a_{\mathrm{n}}3\pi/2|$	$|3(z_4 - z_3)|$	$|3(\rho_5 - \rho_4)|$
$\cos\theta(q)$	$\cos(q3\pi/2)$	0	-1

B.3 Cone

A cone with the same width and length as the capped cylinder in Section B.2 is presented in Figure 23 and is defined by the points $\boldsymbol{r}_1, \boldsymbol{r}_2, \boldsymbol{r}_3$ specified in Table 3. The thickness of the absorber is dented d and the parameters $L_\mathrm{d} = d/\sin(\alpha)$, $a_\mathrm{d} = d/\cos(\alpha)$ are introduced to take this into consideration. The cone is parametrized according to the expressions in Table 4.
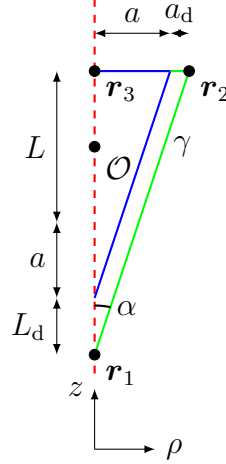
Figure 23: A cone scatterer with total height $L + a$ and width a, coated with an absorber with thickness d.

Table 3: Key points of interest for parametrization of a cone scatterer coated with an absorber.

	$\boldsymbol{r}_1$	$\boldsymbol{r}_2$	$\boldsymbol{r}_3$
ρ_i	0	$a + a_\mathrm{d}$	0
z_i	$-L/2 - a - L_\mathrm{d}$	$L/2$	$L/2$

B.4 Rounded cone

Next we consider a cone with a spherically rounded nose. The underlying cone has the same width and length as the capped cylinder in Section B.2, but the total length of the rounded cone depends on the radius of curvature of the nose. The geometry is presented in Figure 24 and is parametrized through the key points $\boldsymbol{r}_i$, $i = 1, 2, .., 5$. The thickness of the applied absorber is denoted d and the parameters $L_\mathrm{d} = d/\sin(\alpha)$, $a_\mathrm{d} = d/\cos(\alpha)$ are introduced to maintain the absorber thickness along the surface of the scatterer.

Table 4: Parametrization of cone coated with an absorber.

	Cone segment	Flat top
q	$0 \leq q < 1/2$	$1/2 \leq q \leq 1$
$\rho(q)$	$\rho_1 + (\rho_2 - \rho_1)2q$	$\rho_2 + (\rho_3 - \rho_2)(2q - 1)$
$z(q)$	$z_1 + (z_2 - z_1)2q$	z_2
$\hat{\boldsymbol{n}}(q)$	$\dfrac{(z_2 - z_1)\hat{\boldsymbol{\rho}} - (\rho_2 - \rho_1)\hat{\boldsymbol{z}}}{\sqrt{(z_2 - z_1)^2 + (\rho_2 - \rho_1)^2}}$	$\hat{\boldsymbol{z}}$
$\mathrm{d}\ell/\,\mathrm{d}q$	$2\sqrt{(z_2 - z_1)^2 + (\rho_2 - \rho_1)^2}$	$2\lvert\rho_3 - \rho_2\rvert$
$\cos\theta(q)$	$\dfrac{\rho_2 - \rho_1}{\sqrt{(z_2 - z_1)^2 + (\rho_2 - \rho_1)^2}}$	-1

Table 5: Key points of interest for parametrization of a rounded cone scatterer coated with an absorber.

	$\boldsymbol{r}_1$	$\boldsymbol{r}_2$	$\boldsymbol{r}_3$	$\boldsymbol{r}_4$	$\boldsymbol{r}_5$
ρ_i	0	ρ_2	0	$a + a_{\mathrm{d}}$	0
z_i	$-L/2 - a - L_{\mathrm{d}}$	z_2	z_3	$L/2$	$L/2$

In order to parametrize the scatterer we need to determine the coordinates of the center of the spherical nose, as well as the intersecting point between the spherical nose and the cone in such a way that the first order derivative is continuous at this point. This point, denoted $\boldsymbol{r}_2$, is given by the relations

$$\rho_2 = \sqrt{\frac{a_{\mathrm{n}2}^2}{\tan(\alpha)^2 + 1}}, \qquad z_2 = z_1 + \frac{1}{\tan(\alpha)}\sqrt{\frac{a_{\mathrm{n}2}^2}{\tan(\alpha)^2 + 1}}, \qquad \text{(B.5)}$$

where $a_{\mathrm{n}2} = a_{\mathrm{n}1} + d$ is the radius of the nose including the absorber coating. From $\boldsymbol{r}_2$ the location of the center of the nose, denoted $\boldsymbol{r}_3$, is calculated using the relations

$$\rho_3 = 0, \qquad z_3 = z_2 + \sqrt{a_{\mathrm{n}2}^2 - \rho_2^2}. \qquad \text{(B.6)}$$

The angle β in Figure 24 defining the nose is given by $\beta = \arcsin(\rho_2/a_{\mathrm{n}2})$, and the key points of the geometry is summarized in Table 5. To parametrize a rounded capped cone as in Figure 24, the parametrization is broken down to three regions

Figure 24: A capped cone scatterer with total height $L+a$ and width a, coated with an absorber with thickness d.

Table 6: Parametrization of the scatterer in Figure 24.

q	Spherical nose $0 < q < 1/3$	Cone segment $1/3 < q < 2/3$	Flat top $2/3 < q < 1$
$\rho(q)$	$a_{n2} \sin(q3\beta)$	$\rho_2 + (\rho_4 - \rho_2)(3q - 1)$	$\rho_4 - \rho_4(3q - 2)$
$z(q)$	$z_3 - a_{n2} \cos(q3\beta)$	$z_2 + (z_4 - z_2)(3q - 1)$	z_4
$\hat{\boldsymbol{n}}(q)$	$\sin(q3\beta)\hat{\boldsymbol{\rho}} - \cos(q3\beta)\hat{\boldsymbol{z}}$	$\dfrac{(z_4 - z_2)\hat{\boldsymbol{\rho}} - (\rho_4 - \rho_2)\hat{\boldsymbol{z}}}{\sqrt{(z_4 - z_2)^2 + (\rho_4 - \rho_2)^2}}$	$\hat{\boldsymbol{z}}$
$\mathrm{d}\ell/\mathrm{d}q$	$a_{n2}3\beta$	$3\sqrt{(z_4 - z_2)^2 + (\rho_4 - \rho_2)^2}$	$3\lvert\rho_4\rvert$
$\cos\theta(q)$	$\cos(3q\beta)$	$\dfrac{3q(\rho_4 - \rho_2)}{\sqrt{(z_4 - z_2)^2 + (\rho_4 - \rho_2)^2}}$	-1

B.5   Capped cone-cylinder

A slightly more complicated structure consisting of a cone and a cylinder is parametrized. The same rounding is introduced in the nose and at the wedge in the middle of the structure, see Figure 25. The nose is parametrized in the same way as in Section B.4 where the spherical nose has the maximum parametrization angle β_1. To determine the location of the center of the upper rounding $\boldsymbol{r}_6$ and the spherical parametrization angle of the upper rounding $2\beta_2$, a number of trigonometric expressions are

introduced:

$$\gamma_1 = \alpha - \pi/2, \qquad \gamma_2 = \alpha/2, \qquad \beta_1 = \arcsin(\rho_2/a_{n2}), \qquad \beta_2 = \pi/2 - \alpha/2,$$

$$x = a_{n2}\sqrt{\frac{1}{\tan(\gamma_2)^2 + 1}\left(1 + \frac{1}{\tan(\gamma_2)^2}\right)} = \frac{a_{n2}}{|\tan\gamma_2|}, \tag{B.7}$$

where γ_1, γ_2 are relevant angles related to the rounding of the edges, and $x = |\boldsymbol{r}_7 - \boldsymbol{r}_4| = |\boldsymbol{r}_5 - \boldsymbol{r}_4|$ is the distance between points of interest. After some calculations, the key coordinates of the geometry in Figure 25 were identified and are summarized in Table 7 where (ρ_1, z_1), (ρ_2, z_2), (ρ_3, z_3) are defined as in (B.5)-(B.6) and in Table 5. From these coordinates is is relatively straightforward to parametrize the scatterer in Figure 25, and the key parameters are presented in Table 8.

Figure 25: A rounded cone-cylinder scatterer with total height $2L + 2a$ and width a, coated with an absorber with thickness d.

Table 7: Key points of interest for parametrization of a rounded cone-cylinder scatterer coated with an absorber.

	$\boldsymbol{r}_1$	$\boldsymbol{r}_2$	$\boldsymbol{r}_3$	$\boldsymbol{r}_4$	$\boldsymbol{r}_5$	$\boldsymbol{r}_6$	$\boldsymbol{r}_7$	$\boldsymbol{r}_8$	$\boldsymbol{r}_9$
ρ_i	ρ_1	ρ_2	ρ_3	$a + d$	$\rho_6 + a_{n2}\cos(\alpha)$	$\rho_4 - a_{n2}$	ρ_4	ρ_4	0
z_i	z_1	z_2	z_3	$L/2 - d\tan(\alpha/2)$	$z_6 - a_{n2}\sin(\alpha)$	$z_4 + x$	z_6	$L/2 + L_{\text{cone}}$	z_8

Table 8: Parametrization of the scatterer in Figure 25.

	Spherical nose	Cone segment
q	$0 \leq q < 1/5$	$1/5 \leq q < 2/5$
$\rho(q)$	$a_{n2} \sin(5q\beta_1)$	$\rho_2 + (\rho_5 - \rho_2)(5q - 1)$
$z(q)$	$z_3 - a_{n2} \cos(5q\beta_1)$	$z_2 + (z_5 - z_2)(5q - 1)$
$\hat{\boldsymbol{n}}(q)$	$\sin(5q\beta_1)\hat{\boldsymbol{\rho}} - \cos(5q\beta_1)\hat{\boldsymbol{z}}$	$\dfrac{(z_5 - z_2)\hat{\boldsymbol{\rho}} - (\rho_5 - \rho_2)\hat{\boldsymbol{z}}}{\sqrt{(z_5 - z_2)^2 + (\rho_5 - \rho_2)^2}}$
$\mathrm{d}\ell/\mathrm{d}q$	$a_{n2}5\beta_1$	$5\sqrt{(z_5 - z_2)^2 + (\rho_5 - \rho_2)^2}$
$\cos\theta(q)$	$\cos(5q\beta_1)$	$\dfrac{5q(\rho_5 - \rho_2)}{\sqrt{(z_5 - z_2)^2 + (\rho_5 - \rho_2)^2}}$

	Rounded edge	Straight cylinder
q	$2/5 \leq q < 3/5$	$3/5 \leq q < 4/5$
$\rho(q)$	$\rho_6 + a_{n2} \cos((5q - 3)2\beta_2)$	ρ_7
$z(q)$	$z_6 + a_{n2} \sin((5q - 3)2\beta_2)$	$z_7 + (z_8 - z_7)(5q - 3)$
$\hat{\boldsymbol{n}}(q)$	$\cos((5q - 3)2\beta_2)\hat{\boldsymbol{\rho}}$ $+ \sin((5q - 3)2\beta_2)\hat{\boldsymbol{z}}$	$\hat{\boldsymbol{\rho}}$
$\mathrm{d}\ell/\mathrm{d}q$	$a_{n2}10\beta_2$	$5(z_8 - z_7)$
$\cos\theta(q)$	$-\sin((5q - 3)2\beta_2)$	0

	Flat top	
q	$4/5 \leq q \leq 1$	
$\rho(q)$	$\rho_8 - \rho_8(5q - 4)$	
$z(q)$	z_8	
$\hat{\boldsymbol{n}}(q)$	$\hat{\boldsymbol{z}}$	
$\mathrm{d}\ell/\mathrm{d}q$	$5\rho_8$	
$\cos\theta(q)$	-1	

C   Full Wave Benchmark Simulations and Mesh Convergence

A capped cylinder with the parameters $a = 4\lambda_0/3$, $L_{\text{tot}} = 16\lambda_0/3$, $w = 8\lambda_0/3$ has been simulated both in FEKO and in Comsol Multiphysics for verification of the simulation results achieved in the 2D axially symmetric solver in Comsol, which is used for most full wave simulations in this work. The structure was simulated both with and without a Salisbury absorber and the results in Figure 26 show good agreement between the softwares. In the right plot in Figure 26 a mesh convergence study is presented, where a PEC capped cylinder of the same size as in the left plot has been simulated using different mesh settings. It can be seen that when 10 steps per wavelength (at the shortest wavelength of the simulation λ_2) mesh setting is used, the agreement is good in comparison to much finer mesh settings.
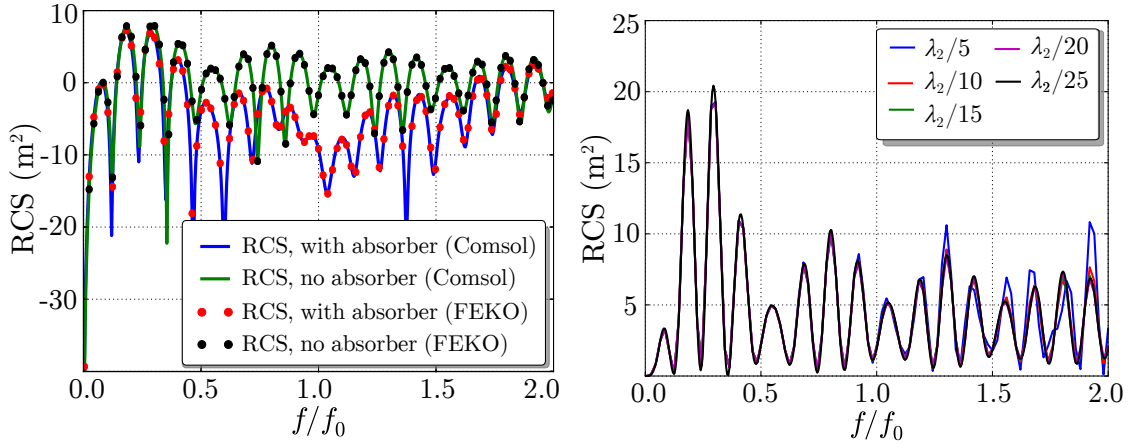

Figure 26: In the left figure a capped cylinder with the parameters $a = 4\lambda_0/3$, $L_{\text{tot}} = 16\lambda_0/3$, $w = 8\lambda_0/3$ has been simulated both in FEKO and in Comsol Multiphysics, using 10 steps per wavelength mesh setting, with and without a Salisbury screen absorber applied. In the right figure a PEC capped cylinder scatterer has been simulated in Comsol using different mesh settings.

References

[1]   S. A. Akhmanov and S. Y. Nikitin. "Physical optics". Clarendon Press, 1997.

[2]   C. A. Balanis. "Antenna Theory". Third. John Wiley & Sons, 2005.

[3]   J. G. van Bladel. "Electromagnetic Fields". Second Edition. IEEE Press, 2007.

[4]   A. Bondeson, T. Rylander, and P. Ingelström. "Computational Electromagnetics". Springer-Verlag, 2005.

[5]   M. Born and E. Wolf. "Principles of optics: electromagnetic theory of propagation, interference and diffraction of light". Elsevier, 2013.

[6] R. Coifman, V. Rokhlin, and S. Wandzura. "The fast multipole method for the wave equation: a pedestrian prescription". *IEEE Antennas Propag. Mag.* 35 (3) (1993): pp. 7–12.

[7] D. B. Davidson. "Computational electromagnetics for RF and microwave engineering". Cambridge University Press, 2005.

[8] O. Ergul and L. Gurel. "The multilevel fast multipole algorithm (MLFMA) for solving large-scale computational electromagnetics problems". John Wiley & Sons, 2014.

[9] A. Ericsson, J. Lundgren, and D. Sjöberg. "Experimental characterization of circular polarization selective structures using linearly single-polarized antennas". *IEEE Transactions on Antennas and Propagation* 65 (8) (2017): pp. 4239 –4249.

[10] A. Ericsson, D. Sjöberg, C. Larsson, and T. Martin. *Scattering from a multilayered sphere - Applications to electromagnetic absorbers on double curved surfaces.* Tech. rep. LUTEDX/(TEAT-7249)/1–33/(2017). Lund University, 2017.

[11] A. Ericsson and D. Sjöberg. "Design and analysis of a multilayer meander line circular polarization selective structure". *IEEE Trans. Antennas Propag.* 65 (8) (2017): pp. 4089–4101.

[12] A. Ericsson, D. Sjöberg, C. Larsson, and T. Martin. "Scattering for doubly curved functional surfaces and corresponding planar designs". In: *Antennas and Propagation (EuCAP), 2016 10th European Conference on.* IEEE. 2016, pp. 1–2.

[13] M. Ferrando-Bataller, F. V. Bondìa, and A. Valero-Nogueira. "Fast physical optics for smooth surfaces". In: *Proceedings of the Fourth European Conference on Antennas and Propagation.* 2010, pp. 1–3.

[14] P. R. Foster. "The region of application in GTD/UTD". In: *1996 Third International Conference on Computation in Electromagnetics (Conf. Publ. No. 420).* 1996, pp. 382–386.

[15] E. Garcia, C. Delgado, L. Lozano, I. Gonzalez-Diego, and M. F. Catedra. "An efficient hybrid-scheme combining the characteristic basis function method and the multilevel fast multipole algorithm for solving bistatic rcs and radiation problems". *Progress In Electromagnetics Research B* 34 (2011): pp. 327–343.

[16] W. C. Gibson. "The method of moments in electromagnetics". Vol. 1. Chapman & Hall/CRC London, UK, 2008.

[17] J. M. Jin. "Theory and Computation of Electromagnetic Fields". Wiley, 2011.

[18] E. Jones, T. Oliphant, P. Peterson, et al. *SciPy: Open source scientific tools for Python.* 2001.

[19] J. B. Keller. "Geometrical theory of diffraction". *J. Opt. Soc. Am.* 52 (1962): pp. 116–130.

[20] E. F. Knott, J. F. Shaeffer, and M. T. Tuley. "Radar Cross Section". SciTech Publishing Inc., 2004.

[21] R. Maaskant, R. Mittra, and A. Tijhuis. "Fast analysis of large antenna arrays using the characteristic basis function method and the adaptive cross approximation algorithm". *IEEE Trans. Antennas Propag.* 56 (11) (2008): pp. 3440–3451.

[22] R. Mittra and K. Du. "Characteristic basis function method for iteration-free solution of large method of moments problems". *Progress In Electromagnetics Research B* 6 (2008): pp. 307–336.

[23] K. Mitzner. *Incremental length diffraction coefficients*. Tech. rep. DTIC Document, 1974.

[24] X.-M. Pan, L. Cai, and X.-Q. Sheng. "An efficient high order multilevel fast multipole algorithm for electromagnetic scattering analysis". *Progress In Electromagnetics Research* 126 (2012): pp. 85–100.

[25] G. T. Ruck, D. E. Barrick, W. D. Stuart, and C. K. Krichbaum. "Radar Cross-Section Handbook". Vol. 1 and 2. Plenum Press, 1970.

[26] T. Shijo, L. Rodriguez, and M. Ando. "The modified surface-normal vectors in the physical optics". *IEEE Transactions on Antennas and Propagation* 56 (12) (2008): pp. 3714–3722.

[27] D. Sjöberg and A. Ericsson. *Computation of radar cross section using the physical optics approximation*. Tech. rep. LUTEDX/(TEAT-7255)/1–16/(2017). Lund University, 2017.

[28] D. G. Smith. "Field Guide to Physical Optics". SPIE Press, 2013.

[29] O. N. Stavroudis. "The Mathematics of Geometrical and Physical Optics: the k-function and its Ramifications". John Wiley & Sons, 2006.

[30] P. Y. Ufimtsev. *Method of edge waves in the physical theory of diffraction*. Tech. rep. DTIC Document, 1971.

[31] P. Y. Ufimtsev. "Fundamentals of the physical theory of diffraction". John Wiley & Sons, 2007.

[32] Y. Z. Umul. "Modified theory of physical optics". *Opt. Express* 12 (20) (2004): pp. 4959–4972.